University of California

Los Angeles

Dislocation-Based Crystal Plasticity Finite Element Modelling of Polycrystalline Material Deformation

A dissertation submitted in partial satisfaction

of the requirements for the degree

Doctor of Philosophy in Material Science and Engineering

by

Chunlei Liu

2006

The dissertation of Chunlei Liu is approved.

Jenn-Ming Yang

Jiun-Shyan Chen

Nasr M. Ghoniem, Committee Chair

University of California, Los Angeles

2006

To my dear wife Wei and our beloved son Jiaju. To my parent who raised me in a small village in north China, and told me always to be useful to others and the society.

Table of Contents

List of Figures

List of Tables

Acknowledgments

I want to thank Professor Ghoniem for his generous support and insightful guidance during my research. I also would like to extend my appreciation to other members on my doctoral committee, Professor A. Ardell, Professor J. Chen and Professor J. Yang, for their efforts and time to participate in my oral exam and final defense. My thanks also go to Professor J. Ju, Professor E. Taciroglu and Professor W. Klug for their generous helps with my research. Finally, I would like to express my thanks to everyone in the Computational Nano&Micro Mechanics Lab: Aaron, Jafaar, Lan, Tamer, Ben, Qingyang, Michael, Silvester, Giacomo and Ming, for the great time we spent together.

Vita

1972	Born, Kulun Qi, Inner Mongolia, China.
1990-1995	B.S., (Material Science and Engineering), Beijing University of Aeronautics and Astronautics, China
1995–2002	Structural Engineer, Guangzhou Aircraft Maintenance Engineering Co. Ltd., China
2002-2003	M.S., (Material Science and Engineering), University of California, Los Angeles, USA.
2003-2006	Ph.D., (Material Science and Engineering), University of California, Los Angeles, USA.

Abstract of the Dissertation

Dislocation-Based Crystal Plasticity Finite Element Modelling of Polycrystalline Material Deformation

by

Chunlei Liu

Doctor of Philosophy in Material Science and Engineering

University of California, Los Angeles, 2006

Professor Nasr M. Ghoniem, Chair

The objective of this research is to develop an understanding of the mechanical behavior and dislocation microstructure evolution of copper single and polycrystals, and to delineate the physical and mechanical origins of spatially-localized plastic deformation. Traditional approaches to the study of plastic instabilities have either been based on kinematic considerations, such as finite strain effects and geometric softening, or physics-based concepts. In this study, we develop a framework that combines both approaches. A rate-independent crystal plasticity model was developed to incorporate micromechanics, crystallinity and microstructure into a continuum description of finite strain plasticity. A comprehensive dislocation density model based on rate theory is employed to determine the strain hardening behavior within each plastic slip system for the fcc crystal structure. Finite strain effects and the kinematics of crystal plasticity are coupled with the dislocation-density based model via the hardening matrix in crystal plasticity.

ABAQUS/CAE is employed as a finite element method solver, and several

user's subroutines were developed to model fcc crystals with 2 and 12 slip systems. The developed material models are applied to study single and polycrystal deformation behavior of copper. Interfaces between the ABAQUS user's subroutine Umat and the ABAQUS main code are developed to allow further extension of the current method.

The results of the model are first compared to earlier simulations of localized shear bands in a single copper crystal showing the association of the shear band with defects, as illustrated by Asaro. Current simulations for bicrystlas indicate that shear band localization initiates at the triple point junction between the two crystals and the free surface. Simulations carried out for polycrystals clearly illustrate the heterogeneous nature of plastic strain, and the corresponding spatial heterogeneity of the mobile dislocation density. The origins of the spatial heterogenieties are essentially geometric, as a result of constraints on grain rotation (finite strain effects), geometric softening due to plastic unloading of neighboring crystals. The physical origins of plastic instabilities manifest themselves in the coupling between the dislocation densities and the localized kinematically-induced softening.

CHAPTER 1

Introduction and Research Background

Currently, the largest sources of energy are still the combustion of coal, oil and natural gas. As we know, all these energy sources are not re-usable, and they will run out at some future point. An international collaboration project, ITER (International Thermonuclear Experiment Research) has already been launched to build a nuclear fusion experimental device to test the feasibility of fusion energy as a sustainable source for the future. However, the environmental and operational conditions of structural materials in nuclear energy systems are undoubtedly the harshest among any technological applications. These materials must operate reliably for extended periods of time without maintenance or repair. They must withstand high particle and heat fluxes, as well as significant thermal and mechanical forces.

To make sure that a nuclear reactor is safe, research structural analysis of large modules are now routinely performed with the finite element method, as shown in figure 1.1 *b*.

However, understanding the mechanical behavior of materials is essential to computing elastic, plastic deformation, crack initiation and propagation, and any mechanical and thermal load related failures. Recent research is focused on studies of structural materials and evolution of dislocation microstructure with crystal plasticity method as shown in figure 1.1 (*c*) and dislocation dynamics in figure 1.1 (*d*). These methods have been developed to study and explain plastic behav-

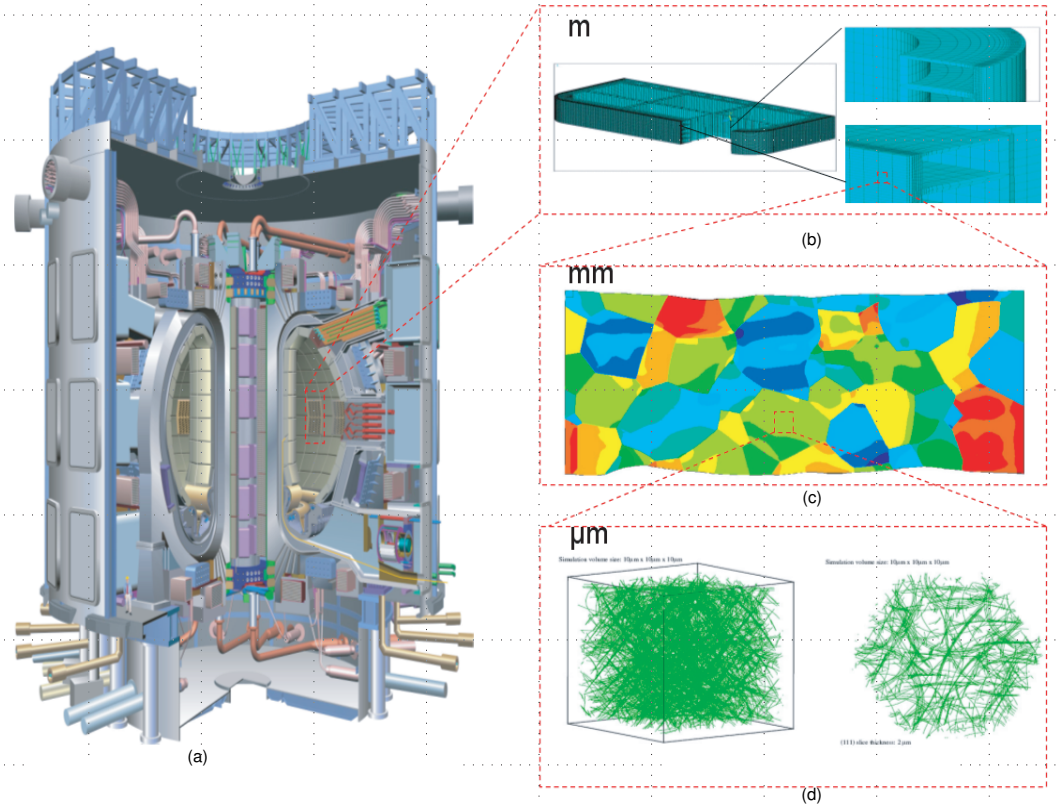

Figure 1.1: Research on nuclear energy system structure and material's mechanical behavior at different length scales. (a). Schematics of nuclear fusion reactor (b). Finite element analysis of nuclear cooling structure (courtesy of professor S. Sharafat). (c). Mechanical behavior study with the polycrystal plasticity method coupled with dislocation density based model (current work). (d). Mechanical behavior study with dislocation dynamics within a single crystal (after Z. Wang. [76])

ior, strain hardening and plastic deformation related dislocation microstructure evolution. These models are applied to the understanding of plastic deformation and failure at different length and time scales.

Crystal plasticity is a method developed to study material's heterogeneous plastic deformation based on modelling plastic slip on different slip systems within the crystal. This method was first formulated by Taylor and Elam [68, 69], and Taylor [72, 71]. Constitutive equations for elasto-plastic behavior of single crystal materials were first formulated by Mandel [44] and Hill [32] based on modern continuum mechanics, and later extended to finite strain formulation by Rice [57], Hill and Rice [31], Asaro and Rice [6], and Asaro [8, 7]. The method of crystal plasticity works well for solving problems of heterogeneous mechanical behavior, and was extensively developed to study heterogeneous plastic deformation, lattice rotation and texture evolution when metals are subjected to large deformation, or to solve related practical problems met in manufacturing processes like metal rolling and forming.

Keeping all advantages of crystal plasticity for studying heterogeneous plasticity and also to make it possible to study dislocation microstructure evolution at the same time. We developed a method to couple polycrystal plasticity with dislocation density based model, which builds the correlation between strain hardening effects in crystal plasticity and dislocation density evolution.

We built a model to study the mechanical behavior and dislocation microstructure evolution of unirradiated OFHC, (Oxygen-Free High Conductivity)-copper, containing Ag, Si, Fe and Mg with concentrations of 10 ppm, 3 ppm, less than 1 ppm and less than 1 ppm, respectively (as shown in figure 1.2 [65]). Since the amount of alloying elements is very small, material is assumed to be pure copper. In our modelling, we performed the following:

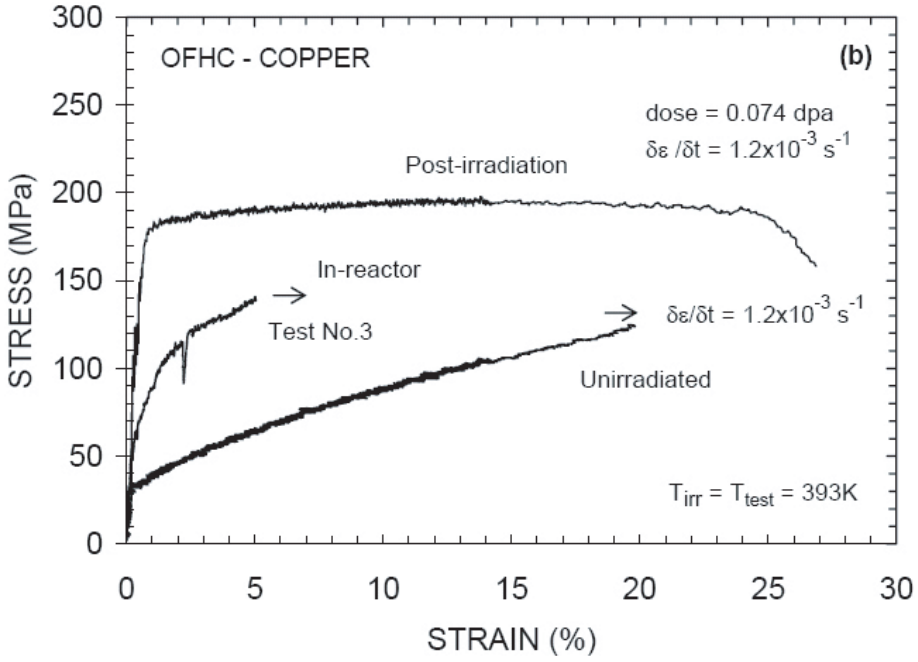

Figure 1.2: Strain stress curve of OFHC-Copper from experiments. This figure is adopted from Singh's Report [65]

1. Single and polycrystal plasticity formulation and implementation using finite element method with developing users material subroutine UMAT in ABAQUS.

2. Further development of the Ghoniem-Matthews-Amodels (GMA) [25] dislocation density based material model to define the strain hardening in each slip system.

3. Coupling the dislocation density based material model with crystal plasticity within the finite element framework to study heterogeneous plasticity behavior and dislocation microstructure evolution during plastic deformation in copper.

In this dissertation, experimental observations are introduced in chapter 2. A review of previous research on crystal plasticity and heterogeneous deformation is given in chapter 3. Our modelling of crystal plasticity and the coupling method are developed in chapter 4. the dislocation density based material model defining the self-hardening for crystal plasticity is discussed in chapter 5. Results of simulation of $3D$ model with 2 and 12 slip system are shown and discussed in chapter 6. Research achievements are summarized in chapter 7. Since our developed model could be further extended to couple more comprehensive dislocation based model or integrate damage models to study post-irradiation material follow-up research is proposed in chapter 7.

CHAPTER 2

Overview of Experimental Results

The localized nature of plastic deformation and the connection between plasticity and slip on crystallographic orientations were documented as early as 1898 [23]. Figure 2.1 adapted from the work of Ewing and Rosenhain, shows that a material subjected to simple shear deforms plastically and formes steps on the surface. They gave the following detailed description: "The diagram, fig. 15, is intended to represent a section through the upper part of two contiguous surface grains, having cleavage or gliding places as indicated by the dotted lines, AB being a portion of the polished surface, C being the junction between the two grains. When the metal is strained beyond its elastic limit, as say by a pull in the direction of the arrows, yielding takes place by finite amounts of slips at a limited number of places, in the manner shown at a, b, c, d, e. This exposed short portions of inclined cleavage or gliding surface, and when viewed in the microscope." They clearly described that plastic slip is preferred along certain crystallographic directions.

They concluded that that grains were crystals with more or less homogeneous crystallographic orientation. To some extents, this explains that plastic slip steps are along similar crystallographic directions within same grain, and might be not the same in the neighboring grains as shown in figure 2.2.

Later on, experimentalists observed more heterogeneous plastic deformation within metals. As shown in figure 2.3, Elam [21] observed the formation of shear bands which sustain much larger plastic strain than the surrounding area within a

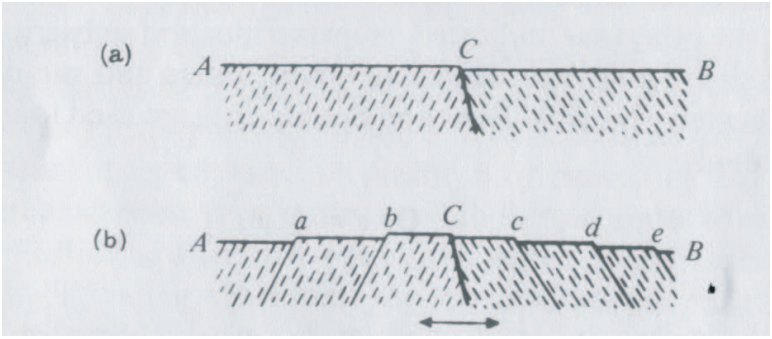

Figure 2.1: Schematic diagram adopted from Ewing and Rosenhain (1900)[23]

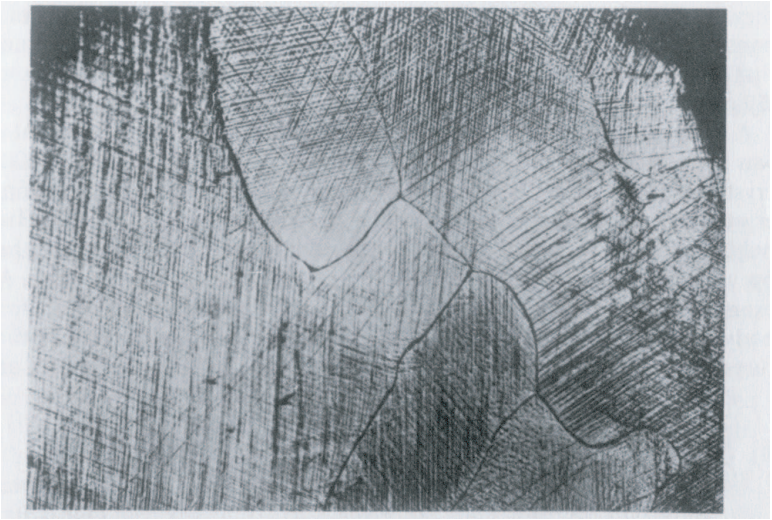

Figure 2.2: Optical micrograph of deformed ploycrystalline lead adopted from Ewing and Rosenhain [23]

single crystal of aluminum 2.8%wt copper alloy subjected to tensile stress. Large lattice rotations of $10^\circ - 20^\circ$ within the shear band were observed.

Figure 2.3: Single crystal of aluminum 2.8%wt copper alloy deformation in tension. [21]

Morii and Nakayama [48] found that shear bands appeared in copper when subjected to a shear stress. Figure 2.4 is an electron micrograph that shows the formation of a shear band within a single crystal of copper and also the dislocation sub-grain structure developing within the shear band.

Heterogeneous plastic behavior and related microstructure evolution have been observed not only in single crystals, but also in polycrystals.

Diliamore *et al.* in 1979 observed the formation of shear bands in heavily rolled polycrystalline aluminum-4.75%wt copper alloy. Figure 2.5 shows that shear bands formed roughly along $+45^\circ$ and -45° due to the reorientation of grains caused by the rolling process. This shows that shear bands can also be formed within polycrystals. Surface roughness caused by large local plastic slips was also observed.

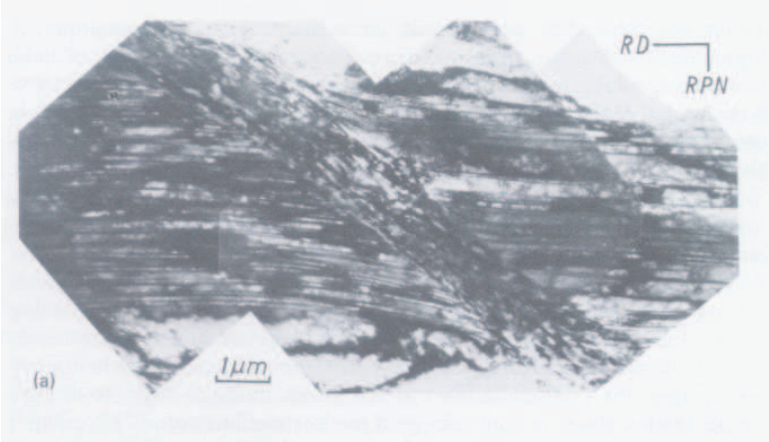

Figure 2.4: A shear band formed during the plain strain rolling of a single crystal of copper. [48]

Figure 2.5: An optical micrograph of shear bands developed in plane strain rolling of a polycrystalline aluminum $-4.75\%wt$ copper alloy [20]

Since dislocation motion within the material is closely related to the ability of the material to deform plastically, the dislocation microstructure evolution has also been studied for many years. Singh *et al.* observed a heterogeneous distribution of dislocations when the material was subjected to large plastic deformation. Figure 2.6 shows different dislocation microstructure were formed under different level of plastic deformation.

These heterogeneous plastic deformation, large lattice rotation and dislocation microstructure evolution observed in experiments cannot be explained by well-developed isotropic plasticity theory. Many methods at different physical scales have been developed to explain these phenomena and to model this heterogeneous mechanical behavior. Most of these theories work well at certain scales or explain certain experimental observations to some extent. The details of some representative models will be introduced in the next chapter and comparison of these models will also be done.

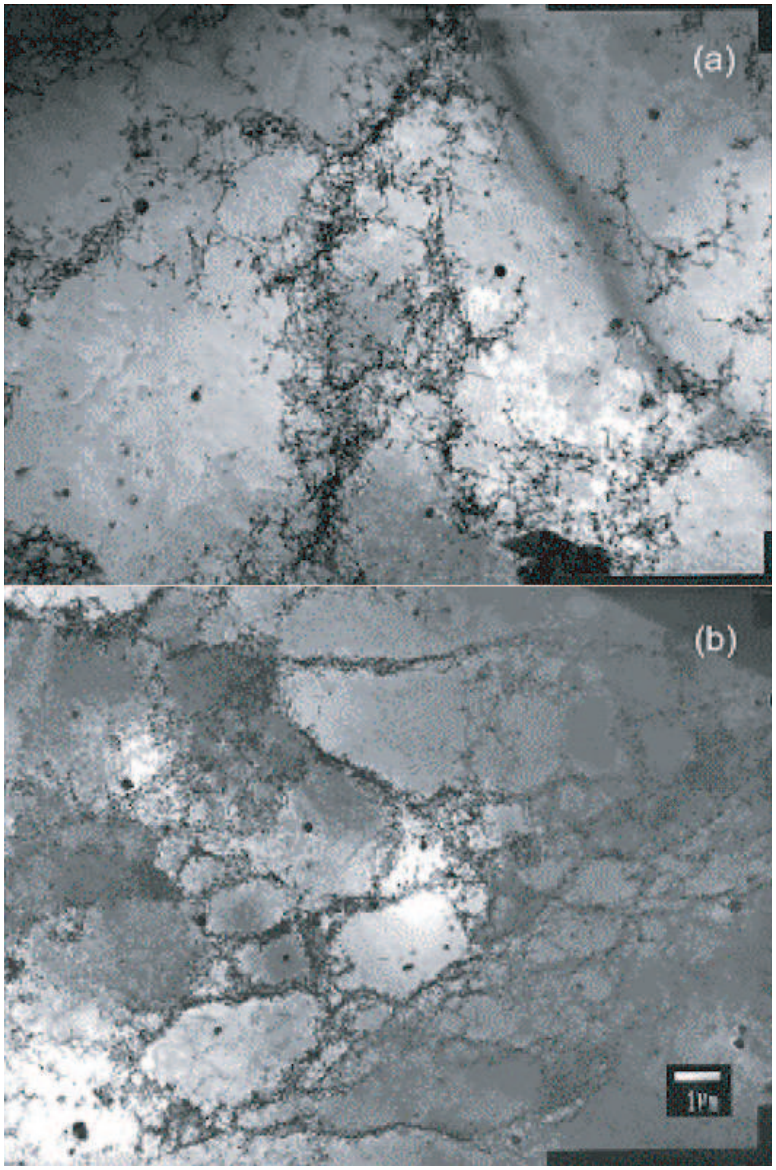

Figure 2.6: Dislocation microstructure in the unirradiated copper specimens tensile tested at a strain rate of $1.3 \times 10^{-7} s^{-1}$ to a total strain of (a) 4%. Segregation of dislocations (b)20%. Formation of dislocation cells.)[65]

CHAPTER 3

Review of Computational Plasticity

In this chapter several methods of computational plasticity are reviewed. Macroscopic plasticity theory of isotropic/kinematic hardening is introduced since this method builds the main computational framework. The formulation of crystal plasticity is then reviewed. A brief introduction to modelling strain hardening effects with the dislocation theory is also given at the last section of this chapter.

3.1 Isotropic/Kinematic Plasticity

3.1.1 Fundamental Theory of Plasticity

Numerical formulation of $3D$ general isotropic plasticity will be discussed in the section since modelling isotropic plasticity for finite element method lays down theoretical foundation for all other plasticity modelling. Later on, it will be found that the main differences between isotropic plasticity and crystal plasticity are flow rule and shape of yield surface.

The finite element method is the main method to obtain the numerical solution for a nonlinear boundary value problem by solving a discretized momentum balance equation by iteration. Generally, There are three steps involved in a finite element code:

- The discretized global momentum equations generate incremental displace-

ments, and incremental strains can be derived from these known displacements. Normally, this strain is called the trial strain since most finite element code today is strain-driven.

- New state variables $[\sigma,\ \varepsilon^p, q]$ at step $n+1$ can be obtained by solving nonlinear equation of local constitutive equations based on known initial values of variables, which are also the solution of step n.

- Then, the discretized global momentum equations are tested for the stress computed from this step. If the global balance is satisfied, go to next step. If the global balance is not satisfied, go back to the very beginning of step $n+1$, and test another set of trail displacements until the momentum equations are balanced.

The nonlinearity of the computational system due to materials' nonlinear behavior is solved at the second step based on constitutive equations at the local level. In the first and third step to trial values of displacements are applied and the global momentum balance of the system is tested at the global level by the displacement-driven finite element method.

To solve the local material nonlinear behavior, the classical redial return algorithm was first put forward by Wilkins [79]. Krieg and Krieg[38] summarized the formulation of the return mapping method to replace the classical method based on elasto-plastic tangent modulus. Details of these numerical algorithms will not be discussed (see reference [63] for details). Plasticity theory based on J_2 theory will be discussed here.

3.1.1.1 Yield function

For isotropic materials, plastic deformation starts when the following function Eq. 3.1 is satisfied. This function is called yield function:

$$F(\sigma, R) = 0 \tag{3.1}$$

Where R is internal state variable.

For general isotropic/kinematic von Mises yield condition, the yield function is defined as Eq. 3.3 and flow rule defined as Eq. 3.4, internal state hardening variable $\mathbf{q} := (\alpha, \beta)$. α is the equivalent plastic strain which defines the radius of von Mises yield surface of isotropic hardening, and β defines the center of von Mises yield surface in deviatoric stress space. γ is the plastic increment in current step.

$$\begin{aligned} v &= dev[\sigma] - \beta & (3.2)\\ f(\sigma, q) &= \|v\| - \sqrt{\frac{2}{3}} K(\alpha) & (3.3)\\ \dot{\varepsilon}^p &= \gamma \frac{v}{\|v\|} & (3.4)\\ \dot{\beta} &= \gamma \frac{2}{3} H(\alpha) \frac{v}{\|v\|} & (3.5)\\ \dot{\alpha} &= \gamma \sqrt{\frac{2}{3}} & (3.6) \end{aligned}$$

Where, $K(\alpha)$ function is called isotropic hardening modulus and $H(\alpha)$ function is called kinematic hardening modulus. equivalent plastic strain is defined as:

$$\alpha = \int_0^t \sqrt{\frac{2}{3}} \|\dot{\varepsilon}^p(\tau)\| d\tau \tag{3.7}$$

Continuum elasto-plastic tangent modulus is defined by:

$$\mathcal{C}^{ep} = \kappa \mathbf{1} \otimes \mathbf{1} + 2\mu[\mathbf{I} - \frac{1}{3}\mathbf{1} \otimes \mathbf{1} - \frac{\mathbf{n} \otimes \mathbf{n}}{1 + \frac{H+K}{3\mu}}] \tag{3.8}$$

Where, $\mathbf{1}$ is second order identity tensor and $\mathbf{I}$ is fourth order identity tensor, $\mathbf{n}$ is flow rule.

3.1.1.2 Algorithm for solving yield function at local material point

To solve the nonlinear yield equation at the local level before testing the global momentum equilibrium in the finite element code, the algorithm in incremental style is summarized by the following steps

1. Apply trial strain and compute stress:

$$\begin{aligned} e_{n+1} &= \varepsilon_{n+1} - \frac{1}{3}(tr[\varepsilon_{n+1}])1 && (3.9)\\ s^{trial}_{n+1} &= 2\mu(e_{n+1} - e^p_n) && (3.10)\\ \eta^{trial}_{n+1} &= s^{trial}_{n+1} - \beta_n && (3.11) \end{aligned}$$

2. Check yield function:

$$\begin{aligned} f^{trial}_{n+1} : &= \|\eta^{trial}_{n+1}\| - \sqrt{\frac{2}{3}}K(\alpha_n) && (3.12)\\ \text{If} \quad f^{trial}_{n+1} &\leq 0 \quad \text{Then} && (3.13)\\ \text{Set}(\cdot)_{n+1} &= (\cdot)^{trial}_{n+1} \quad \text{and Exit} && (3.14)\\ \text{Endif} & && (3.15) \end{aligned}$$

3. Compute the flow rule and $\Delta\gamma$ by solving nonlinear yield function, and update flow rule and equivalent plastic strain:

Solving nonlinear yield function:

(a) Use the solution from the last step as the initial value:

$$\Delta\gamma^{(0)} = 0 \tag{3.16}$$

$$\alpha_{n+1}^{0} = \alpha_0 \tag{3.17}$$

(b) Solve nonlinear equation with Newton method:

i. Do Until:

$$|f(\Delta\gamma^k)| < TOL \tag{3.18}$$

$$k \leftarrow k+1 \tag{3.19}$$

ii. Compute $\Delta\gamma^{(k+1)}$:

$$\begin{aligned} f(\Delta\gamma^k) := & -\sqrt{\frac{2}{3}}K(\alpha_{n+1}^{(k)}) + \|\eta_{n+a}^{trial}\| - \{2\mu\Delta\gamma^{(k)} \\ & +\sqrt{\frac{2}{3}}[H(\alpha_{n+1}^{(k)}) - H(\alpha_n)]\} \end{aligned} \tag{3.20}$$

$$Df(\Delta\gamma^{(k)} := -2\mu\{1 + \frac{H'[\alpha_{n+a}^{(k)}] + K'[\alpha_{n+1}^{(k)}]}{3\mu}\} \tag{3.21}$$

Solve:

$$\Delta\gamma^{(k+1)} = \Delta\gamma^{(k)} - \frac{f[\Delta\gamma^{(k)}]}{Df[\Delta\gamma^{(k)}]} \tag{3.22}$$

iii. Update equivalent plastic strain:

$$\alpha_{n+1}^{(k+1)} = \alpha_n + \sqrt{\frac{2}{3}}\Delta\gamma^{(k+1)} \tag{3.23}$$

After the internal convergence is achieved, update flow rule and equivalent plastic strain.

$$n_{n+1} := \frac{\eta_{n+1}^{trial}}{\|\eta_{n+1}^{trial}\|} \tag{3.24}$$

$$\alpha_{n+1} := \alpha_n + \sqrt{\frac{2}{3}}\Delta\gamma \tag{3.25}$$

4. Update plastic strain and correct elastic strain to obtain the correct stress:

$$\beta_{n+1} = \beta_n + \sqrt{\frac{2}{3}}[H(\alpha_{n+1}) - H(\alpha_n)]n_{n+1} \tag{3.26}$$

$$e^p_{n+1} = e^p_n + \Delta\gamma n_{n+1} \tag{3.27}$$

$$\sigma_{n+1} = \kappa \mathbf{tr}[\varepsilon_{n+1}]1 + s^{trial}_{n+1} - 2\mu\Delta\gamma n_{n+1} \tag{3.28}$$

5. Update consistent elastoplastic tangent moduli (The continuum elastoplastic tangent moduli defined by Eq. 3.8 does not give a quadratic convergence rate, but it is easier to compute.):

$$\mathcal{C}_{n+1} = \kappa \mathbf{1} \otimes \mathbf{1} + 2\mu\theta_{n+1}[\mathbf{I} - \frac{1}{3}\mathbf{1} \otimes \mathbf{1}] - 2\mu\bar{\theta}_{n+1}\mathbf{n}_{n+1} \otimes \mathbf{n}_{n+1} \tag{3.29}$$

$$\theta_{n+1} := 1 - \frac{2\mu\Delta\gamma}{\|\eta^{trial}_{n+1}\|} \tag{3.30}$$

$$\bar{\theta_{n+1}} := \frac{1}{1 + \frac{[K'+H']_{n+1}}{3\mu}} - (1 - \theta_{n+1}) \tag{3.31}$$

3.2 Crystal Plasticity

Isotropic plasticity modelling based on continuum theory combined with return mapping algorithm provide robust numerical method to solve nonlinear boundary value problems caused by material non-linearities with the finite element method, and it also provides theoretical guidance for building other types of nonlinear plastic models. However, isotropic plasticity is not able to model heterogeneous plastic behavior observed in experiments. To solve this problem, the first model was put forward by Schmid [60] as shown in figure 3.1. This figure shows the deformation process of single crystal. Not only sliding between slip plane occurs, also does lattice rotation if the traction boundary is not changed.

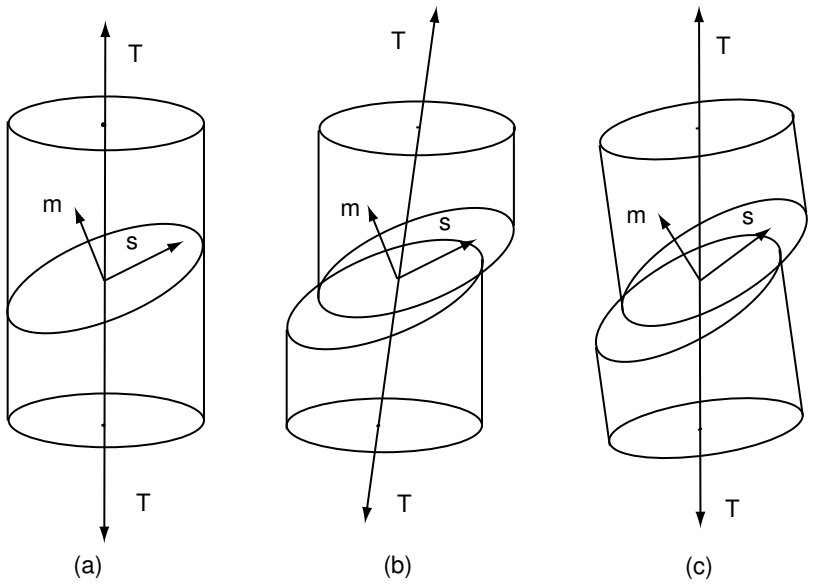

Figure 3.1: Schematic diagrams for a crystal undergoing single slip in tension

The method to describe plastic deformation by crystallographic slip was formulated by Taylor and Elam [68, 69], and Taylor [72, 71]. Constitutive equations for elastoplastic behavior of single crystal material were first formulated by Mandel [44] and Hill [32] based on the modern continuum mechanics, and extended to the finite strain formulation by Rice [57], Hill and Rice [31], Asaro and Rice [6], and Asaro [8, 7]. The modern finite strain crystal plasticity is built closely based on deep understanding on crystal structure, mechanism of plastic slip, theory of dislocation and finite strain kinematics and constitutive behavior. A brief introduction to crystal structure and theory of dislocation will be given here since they are indispensable component to building a crystal plasticity model, especially for the model developed by us, which combines the traditional finite strain crystal plasticity with the dislocation density based model.

3.2.1 Crystal Structure

Most solid metals have crystalline structure, which means that atoms within materials are situated in a repeating array over long range. To describe crystalline structure, atoms are imaged as solid hard balls sitting next to each other with different patterns and the minimum repeating pattern is defined as an unit cell. Crystalline structure with atoms located at each corner of the unit cell and centers of all surfaces is called a face-centered cubic crystalline structure fcc as shown in fig 3.2. Copper, aluminum, and nickel has fcc crystalline structure. Similarly, crystalline structure with atoms sitting on each corner and one positioning at the center of the unit cell is call body-centered cubic crystalline structure bcc. Iron has bcc crystalline structure. Some other metal, like zinc, magnesium, has Hexagonal closed-packed crystalline structure hcp.

Mechanical properties of metals, especially the plastic deformation ability, depend on their crystalline structures. Atoms glides on the certain plane along the certain slip direction, along which gliding atoms meet the minimum resistance. Each slip plane and a slip direction form a slip system . The different crystalline structure has different number of slip systems. fcc crystalline structure has 12 slip systems, which are the combination of slip plane family $\{111\}$ and slip direction family $\langle 110 \rangle$. For bcc crystalline structure, there are 48 slip systems. Generally, gliding resistance in slip systems of fcc crystalline structure is much lower than bcc structure if both materials are pure. This means that atoms within fcc crystalline structure are easier to slide than atoms within bcc crystalline structure, or say materials with fcc crystalline structure is easier to undergo plastic deformation than material with bcc structure does, just like copper, aluminum, sustains better plastic deformation capability than iron.

During early studies on mechanical properties of materials, a great discrep-

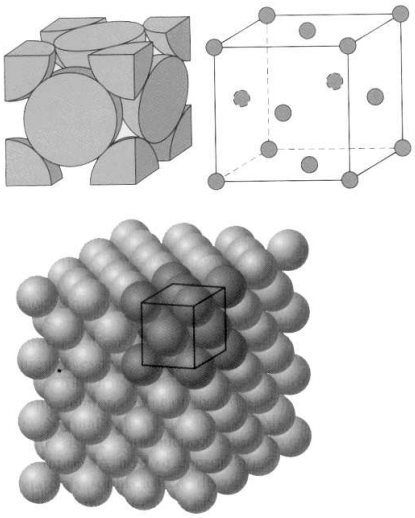

Figure 3.2: Crystal structure of face center cubic . (a). A hard sphere unit cell, each sphere stands for an atom. (b). A reduced-sized sphere unit cell. (c). A fcc crystal structure contains many unit cells. This figure is adopted from [13]

ancy was found between theoretical strength of pure material and strength of real material. During $1930s$, this discrepancy was explained by the defects existing in material, known as dislocations. It was not until $1950s$, dislocations were directly observed with electronic microscope. The theory of dislocations gives scientific explanation to many mechanical phenomena and even makes quantitative estimation of mechanical properties possible. A dislocation is a line defect inside the material. dislocation can be separated as edge dislocation, screw dislocation and mixed dislocation according to difference geometric configuration of defects. Figure3.3 is a schematics of edge dislocation. The direction and magnitude of lattice distortion associated with a dislocation is expressed in terms of a Burgers vector, denoted by a **b**.

Today dislocations can be observed with help of electronic microscope, and

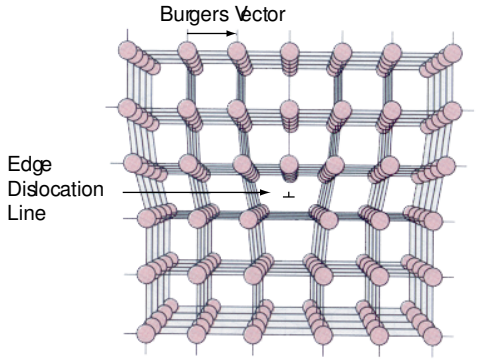

Figure 3.3: Schematics of atomic structure of edge dislocation. [30]

the variations of density of dislocations can be as low as 10^3 mm^{-2} in carefully solidified metal, and as high as 10^9 to 10^{10} mm^{-2} in heavily deformed metals. Figure3.4 shows dislocations in observed in a titanium alloy. The motion of dislocations produce plastic deformation. When the material is subjected to external stress higher than certain level and yields, or say plastic deformation starts, dislocations glide on slip plane along certain slip direction, and this process is called slip. The theory developed to compute plastic deformation within single crystal is call single crystal plasticity theory. Since most metallic materials in use are polycrystalline material as shown in figure 3.5, which means much more grain with different crystalline orientation inside the materials, careful treatment of interaction along grain boundary must be considered to appropriately extend this theory into explanation of plastic behavior in polycrystalline material. Crystal plasticity will be discussed in much more detail in next section and rest of chapters.

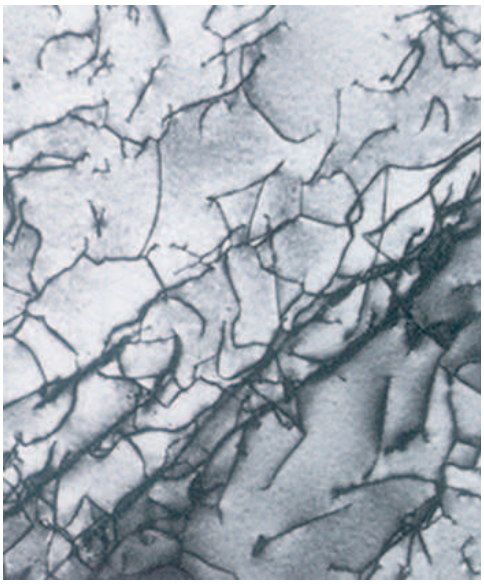

Figure 3.4: A TEM image of titanium alloy, where dislocations are dark lines. 51,450X. This figure is adopted from [13]

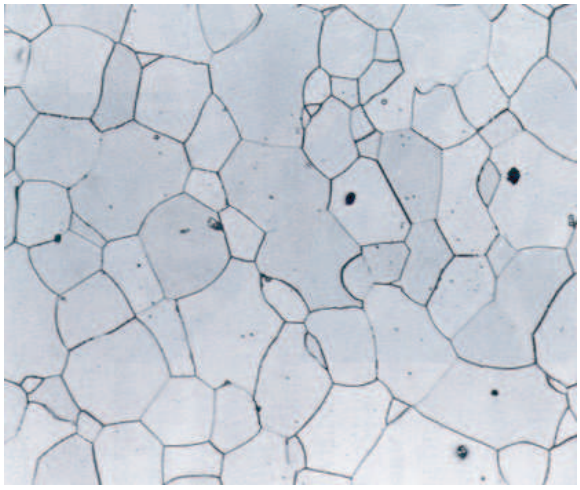

Figure 3.5: An optical microscopic image of the surface of a polished and etched polycrystalline specimen of an iron-chromium alloy, where the grain boundaries are dark lines. This figure is adopted from [13]

3.2.2 Crystal Plasticity Modelling

Although kinematics and constitutive relations were well built for many years. There are three main problems needed to be solved in modern rate-independent theory of crystal plasticity, mainly on how to solve this system. The first is to determine which slip system is active, and the second is to determine the increments of plastic strain in each active slip system. Third, due to the typical multiplicity of slip systems in crystals, the solutions of slip system which satisfys the yield functions systems is not necessarily unique. When the constitutive theory is applied to the numerical solution of boundary value problems, these three features of the rate-independent plasticity theory generally result in numerical problems [3].

The first numerical calculations for a two-dimensional boundary value problem for a rate-independent elastic-plastic single crystal was put forward by Peirce *et al.* [52], whose geometry was idealized in terms of a planar double slip model. Due to the lack of a robust solution strategy to determine the active slip systems and the amount of slip on these systems, the element stiffness matrices become singular for a particular choice of a slip system hardening rule resulting in numerical instabilities. To overcome the limitations of the rate-independent crystal plasticity, Asaro and Needleman [5] developed a rate-dependent crystal plasticity model, which uniquely predicts constitutive response for arbitrary deformation history. Asaro and Needleman (1985) proposed that the shearing rate $\dot{\gamma}^{\alpha}$ on a slip system α is uniquely defined by:

$$\dot{\gamma}^{\alpha} = \dot{\gamma}_0 |\frac{\tau^{\alpha}}{g^{\alpha}}|^{\frac{1}{m}} sign(\tau^{\alpha}) \tag{3.32}$$

In equation 3.32 , τ^{α} is the Schmid shear stress along slip direction, and $s^{\alpha} > 0$

is deformation resistance in this slip system . The parameter $\dot{\gamma_0}$ is a reference shearing rate. And the parameter m stands for the material rate dependence. When $m \rightarrow 0$, the model reproduces the rate-independent plasticity. Plastic strain rate is uniquely determined by this equation, and is proportional to the Schmid shear stress in that slip system. In crystal plasticity theories, the slip system strain hardening g^{α} evolves according to Eq. 3.33.

$$\dot{g^{\alpha}} = \sum_{\beta} h^{\alpha\beta} |\dot{\gamma}^{\beta}| \tag{3.33}$$

where $\dot{\gamma}^{\beta}$ is the plastic incremental rate and the hardening matrix $h^{\alpha\beta}$ defines the rate of hardening effect on slip system α due to plastic increment on slip system β; the diagonal terms define the self-hardening effect and off-diagonal terms define latent-hardening effect of the slip systems. All terms in the hardening matrix $h^{\alpha\beta}$ are deformation history-dependent. As mentioned by Anand *et al* [3], the hardening moduli $h^{\alpha\beta}$ are the least well characterized part of the constitutive equations for crystal elasto-plasticity.

In the rate-dependent formulation of Asaro and Needleman [5], all slip systems are always active and slip at a rate which depends on the resolved shear stress and slip system deformation resistance. Not yield surface is defined. When the resolved stress due to the external force is known, the plastic increment on all slip systems are uniquely determined. In their model, no restriction on the form of the hardening matrix $h^{\alpha\beta}$ is required. There has been considerable recent progress made in the extension and application of the rate-dependent crystal plasticity model of Asaro and Needleman [5] to solve the important boundary value problems (Bronkhorst et al [11].; Anand and Kalidindi [2]), however the rate-dependent constitutive equations for low values of the rate-sensitivity parameter m are very stiff, and the calculations are very time consuming. More

research is still needed to develop a robust calculation scheme to determine the active slip systems, the corresponding plastic increments and the unique solutions for rate-independent theory of crystal plasticity.

To avoid the problem mentioned in rate-dependent problem, *Cuttiño* and Ortiz [18], Anand *et al.* [2, 3], and Miehe *et al.* [47] have done great contributions on formulating a numerical algorithm to solve rate-independent crystal plasticity. Cuitiño and Ortiz [18] proposes an algorithmic setting for a multisurface-type viscoplastic model with elastic domain. Here, the problem of redundant constraints does not occur, due to the viscoplastic regularization effect. Borja and Wren [10] propose a so-called ultimate algorithm for the rate-independent theory which follows the successive development of active slip within a typical discrete time interval. Anand and Kothari [3] solve the system of redundant constraints of rate-independent single-crystal plasticity by using a generalized inverse on the basis of the singular-value decomposition of the Jacobian of the active yield criterion functions. This approach meets the least-square-type optimality conditions by minimizing the plastic dissipation due to the slip activities. Motivated by this development, Schröder and Miehe [61] have proposed an alternative general inverse where the reduced space is obtained by dropping columns of the local Jacobian associated with zero diagonal elements within a standard factorization procedure. In our modelling, the solution approach for true solutions of yield functions proposed by Anand and Kothari [3] was employed.

During the last decade, these solution methods have been further developed and extended to study crystallographic texture and lattice rotation within single and poly crystal under uniaxial monotonic or cyclic loading by P. Dawson *et al* [45, 73, 19, 74] and Y. Huang *et al.* [35] to study strain gradient plasticity. Since the research of Asaro *et al.* [6, 8, 7, 5] provide the main framework of kinemat-

ics and constitutive relations for finite strain crystal plasticity, their theoretical formulations and simulation results is introduced briefly in next section.

3.2.3 Kinematics and Constitutive Relations Formulated by R. Asaro *et al.* [8]

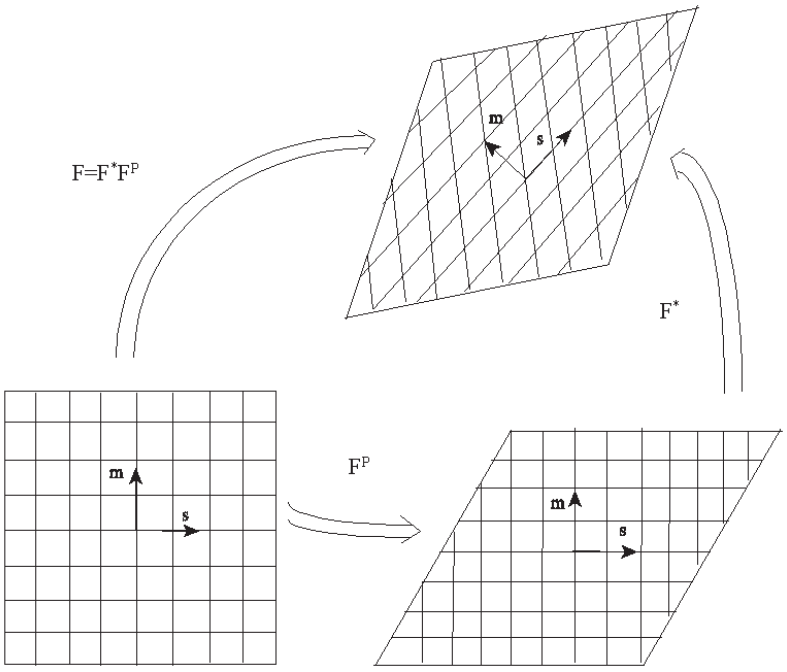

Figure 3.6: Kinematic of elasto-plastic deformation

Figure 3.6 shows the deformation process describe in kinematics formulation. First, the crystal structure undergos pure plastic deformation, then rotation and pure elastic stretching.

The total deformation gradient is split as Eq. 3.34 :

$$F = F^e \cdot F^R \cdot F^p \tag{3.34}$$

Which can also be written as:

$$F = F^* \cdot F^p \tag{3.35}$$

Where, F^p is plastic slip material undergone through the undeformed single crystal lattice, and F^* is deformation gradient caused by rotation and elastic stretching.

The deformation gradient caused by plastic deformation is specified in Eq. 3.36

$$F^p = I + \gamma s \otimes n \tag{3.36}$$

Where, γ is the plastic increment within slip system.

Rotation of slip direction in current coordinate system caused by F^* is specified by Eq. 3.37:

$$s^{'(\alpha)} = F^* \cdot s^{(\alpha)} \tag{3.37}$$

Normal direction of slip plane is also rotated by F^* as specified as by Eq. 3.38

$$m^{'(\alpha)} = m^{(\alpha)} \cdot F^{*-1} \tag{3.38}$$

The velocity gradient in the current coordinate system is:

$$L = \bigtriangledown v = \dot{F}^* \cdot F^{*-1} + F^* \cdot \dot{F}^p \cdot F^{p-1} \cdot F^{*-1} \tag{3.39}$$

Where L can also be expressed as:

$$L = T + S \tag{3.40}$$

Where, T is the symmetric rate of stretching tensor and S is the rate of spin tensor.

T and S are also can be split into plastic slip (T^p,S^p) and lattice deformation (T^*,S^*),

$$T = T^* + T^p \qquad S = S^* + S^p \tag{3.41}$$

In the current coordinate system,

$$T^p + S^p = \sum_{\alpha=1}^{n} \gamma^\alpha s'^{(\alpha)} \otimes m'^{(\alpha)} \tag{3.42}$$

Then, the plastic parts of the rate of spin R^α and the rate of stretching P^α are defined as:

$$R^\alpha = \mathbf{SKEW}(s'^{(\alpha)} \otimes m'^{(\alpha)}) \tag{3.43}$$

$$P^\alpha = \mathbf{SYM}(s'^{(\alpha)} \otimes m'^{(\alpha)}) \tag{3.44}$$

The elastic constitutive relation is specified by:

$$\tau^* = C : T - \sum_{\alpha=1}^{m} (C : P^\alpha + \beta^\alpha)\gamma^\alpha \tag{3.45}$$

Where, τ^* is the rate of change of Kirchhoff stress. C is fourth order elastic moduli tensor, and β^α is defined as:

$$\beta^\alpha = R^\alpha \cdot \tau - \tau \cdot R^\alpha \tag{3.46}$$

Experimental observations of shear band formation and simulation results were published as shown in figure 3.7 in Asaro's [8] and Peirce's *et al* [52] papers. This is first numerical simulation results of formation of shear bands, which agrees with experimental observation very well. There is an initial geometrical imperfection of slight thickness inhomogeneity existing in the model to initiate shear bands and pattern of shear band depends on the configuration of initial imperfections [52].

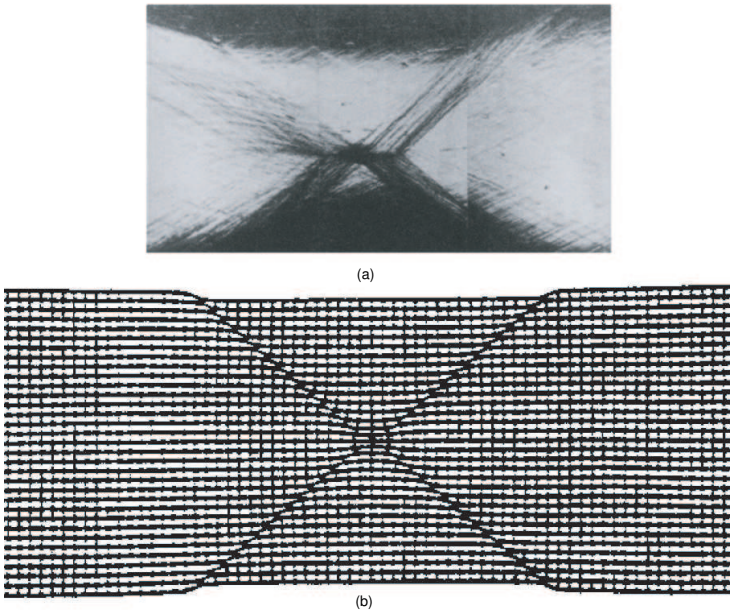

Figure 3.7: (a)Experimental observation of shear band reported formed while material (aluminum 2.8%wt copper alloy) was strain hardening [52]. (b) Shear band formation simulated based Asaros crystal plasticity model with 2 slip systems. [8, 52]

3.3 Modelling the Relationship between Theory of Dislocation and Crystal Plasticity

Asaro's Crystal plasticity provide a very powerful tool to study plastic behavior of material. However, very little physics-based information was directly involved in this model although the model built was closely related experimental measurements [8], and this model is still a pure phenomenological material's constitutive behavior model. Now, As we know, understanding dislocations interaction is essential to studying the physics based mechanism of strain hardening in plas-

ticity. Introduction of dislocation as line defect in crystal was hypothesized by Taylor [70], Orowan [51], and Polanyi [53] even before real dislocations were observed in experiment, to explain the micromechanics of slip with modelling the motion of dislocations embedded in a simple cubic crystal. In the last seventy years, experimental and theoretical development have established the important role of dislocation mechanisms in modelling the strength of materials. However, the lack of powerful computational capability at early years still makes simulate crystal plasticity based on discrete dislocation almost impossible. With the development of bigger and faster computers, it's possible now to bridge the gap between crystal plasticity and dislocation dynamics. To understand modelling strain hardening with the theory of dislocations, a simple model developed by Taylor for explaining the yield strength based on simplified dislocation motion behavior and a comprehensive model based on the modern theory of dislocation dynamics simulation are discussed here.

3.3.1 Yield Strength Model of G. Taylor [70]

Taylor assumed that dislocations are generated at one surface of the crystal and move a distance of x along the slip plane; the maximum value x may have is L, which is either the dimension of the crystal or the distance to a boundary. The average distance dislocations move is then $L/2$. The average spacing between active slip plane is $d/2$, the spacing between dislocations is a, and the average dislocation density ρ is $2/ad$; the shear strain accumulated, γ, is $\frac{1}{2}L^2b/L = Lb/ad$. Since the passing stress is proportional to h^{-1} and h scales with $\rho^{1/2}$ if the dislocation distribution is regular, it follows from dimensional considerations alone that the passing stress is proportional to $\rho^{1/2}$ or actually to $Gb\rho^{1/2}$, and hence to $G(\gamma b/L)^{1/2}$. Finally, if τ_i represents the shear stress required to move an isolated

dislocation, then the stress-strain law derived above has the form:

$$\tau_c = \tau_i + \kappa G(b\gamma/L)^{1/2} = \tau_i + \eta G b \rho^{1/2} \tag{3.47}$$

where κ and η are constants of materials' mechanical properties.

Although distribution of dislocations in Taylor's model is oversimplified, it explains an important source of strain hardening, which is the elastic interaction between dislocations.

3.3.2 Single Crystal Plasticity Model Based on Dislocation Dynamics by Z. Wang and N. Ghoniem [77]

The earliest model based on explicitly computing moving dislocation were put forward in the mid-1980s, in which two dimensional crystal containing multiple dislocations whose behavior was modelled by a set of simplified equations [1, 42]. These simulations provided conceptual framework for simulating strain hardening by dislocation dynamics. However, they cannot directly explain the important features as slip geometry, line tension effects, multiplication, dislocation intersection, or cross-slip, all of them are essential for the formation of dislocation patterns due to limitation of the model built in two dimension. From early 1990s, the development of new computational model for dislocation dynamics in three dimension make it possible to study correlation between dislocation behavior and crystal plasticity by directly simulating the interaction of discrete dislocation motion [39, 34, 62, 76].

In Wang and Ghoniem's model, direct numerical simulation of dislocation motion was employed to study the relationship between the microstructure and macro-scale properties, and improve the understanding of mechanical behavior

of materials. This model could help in designing new materials which are much stronger than materials currently being used by industries within much shorter leadtime by avoiding tedious experimental trial and error process. The DeMecha dislocation dynamics code was applied to study the work-hardening of single crystal copper and obtain the strain-stress curve. Results from their simulation also showed dislocation microstructure of deformed copper.

3.3.2.1 Simulation Procedure in This Model

In this model, a uniaxial tensile stress is applied to simulate the deformation of bulk material. strain is applied ar a constant strain rate in the direction of [100]. The total strain rate is given by:

$$\dot{\varepsilon_{11}} = \dot{\varepsilon_{11}^{e}} + \dot{\varepsilon_{11}^{p}} \tag{3.48}$$

Where $\dot{\varepsilon_{11}^{e}}$ is elastic strain rate and $\dot{\varepsilon_{11}^{p}}$ is plastic strain rate. This plastic strain rate was obtained from the motion of dislocation, given by:

$$\dot{\varepsilon^{p}} = -\frac{1}{2V}\sum_{i=1}^{N}\oint_{0}^{l(i)} v^{(i)}(p)[n^{(i)}(p)\otimes b^{(i)} + b^{(i)}\otimes n^{(i)}(p)]dl \tag{3.49}$$

Where N is number of total dislocation loops, $l^{(i)}$ is the length of dislocation i, V is the volume of the simulated material, n is a unit vector defined as $v \times \xi$, v and ξ are the velocity vector and the tangent vector of the dislocation loop at point p on dislocation lines, respectively.

Then, elastic strain rate can be defined as:

$$\dot{\varepsilon_{11}^{e}} = \frac{\dot{\sigma_{11}}}{E} \tag{3.50}$$

Where E is Young's modules and σ is stress.

Strain-strain curve is derived as:

$$\dot{\sigma_{11}} = E(\dot{\varepsilon_{11}} - \dot{\varepsilon_{11}^{p}}) \tag{3.51}$$

Results from this simulation give the strain-stress curve of copper as shown in figure 3.8, and an embryonic microstructure of cells was obtained, as shown in figure 3.9.

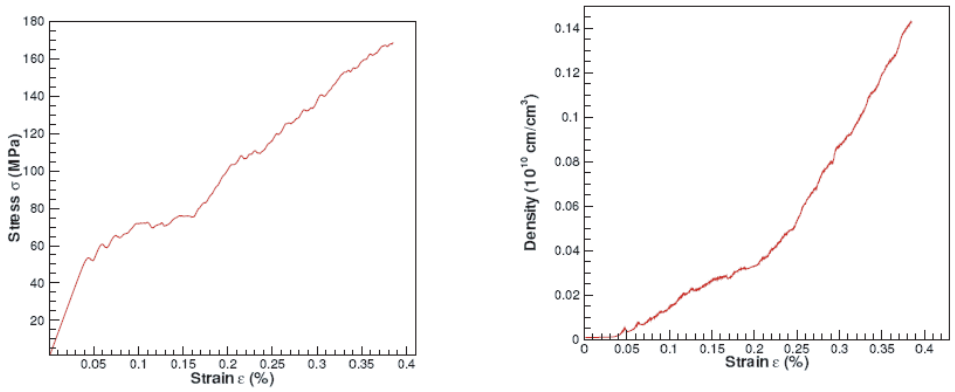

(a) (b)

Figure 3.8: (a). Simulated strain-stress curve, (b). Dislocation density vs. strain. Both of these two figures are adopted from Dr. Z. Wang's Ph.D. Dissertation [77].

This model provides a physically-based fundamental approach to explain how dislocation motion and density affect the mechanical behavior of materials, and also to show the formation of dislocation microstructure by directly simulating the motion and interaction between discrete dislocations. However, keeping track of multiple dislocations and their complex interaction is a daunting task that limits this method to small scale and make the simulation of polycrystal crystal plasticity almost impossible with current computational capabilities.

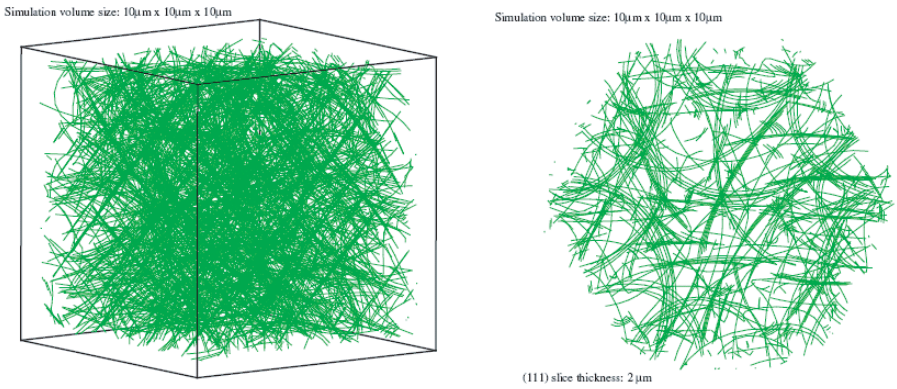

Figure 3.9: (a). Simulated microstructure at strain of 0.2%, (b). Sliced view of microstructure. Both of these two figures are adopted from Dr. Z. Wang's Ph.D. Dissertation [77].

3.4 Comparison between Numerical Methods for Studying Plasticity

By far, isotropic plasticity, pure crystal plasticity and single crystal plastic behavior studied with dislocation dynamics have already been discussed. These methods work very well within certain length scale or solve specific problems. To resolve heterogeneous plastic deformation and the distribution of dislocations within single and polycrystals, we develop here a numerical method coupling crystal plasticity with dislocation density based constitutive equations. A comparison between the current plasticity models is given below.

- Isotropic plasticity (von Mises):
  - Advantages:

1. Model works very well in large scale plastic deformation of ductile materials.
2. Simple formulation, only one yield function needs to be solved at each iteration
3. Computational task is low

- Disadvantages: Not able to explain any local anisotropic behavior

- Crystal plasticity:
  - Advantages:
    1. Able to explain anisotropic plastic behavior observed in experiment.
    2. The global kinematics and constitutive relations are based on confined plastic slip on each slip system. The method clearly shows the influence of crystal structure on plastic deformation.
  - Disadvantages:
    1. Lack of physics explanation underlying the continuum-based model to define the hardening laws within and among slip systems.
    2. The computational task is more intensive, with 12 yield functions to be solved at each iteration and a complicated numerical approach is needed to obtain the solution.

- Dislocation dynamics:
  - Advantages:
    1. Very few assumptions are involved in directly computing the interaction between discrete dislocations.

2. Provides physics-based explanation for strain hardening and microstructure evolution.

- Disadvantages: Extremely computational intensive with a huge demands for CPU time. This also is the main obstacle to expand the method into large scale simulations of Polycrystal plasticity.

- Crystal plasticity coupled with dislocation density-based modelling:

  - Advantages:

    1. The method is able to simulate large scale dislocation microstructure evolution within polycrystals with self-hardening.
    2. Directly describes the spatial distribution of dislocation density.
    3. The method retains all the all advantages of crystal plasticity

  - Disadvantages:

    1. Does not allow for studies of the interaction between discrete dislocations.
    2. The computational task is higher than the traditional crystal plasticity because the dislocation density based subroutine is called at every integration point.

As mentioned above, the biggest advantage of the present model, which couples crystal plasticity with dislocation density is that it keeps all advantages of crystal plasticity, and at the same time integrates the concurrent dislocation microstructure evolution. The details of the present formulation will be discussed in the next two chapters.

CHAPTER 4

A New Method to Couple Crystal Plasticity and Dislocation Microstructure Evolution

4.1 Introduction

We'll develop a new method of coupling crystal plasticity with dislocation density based constitutive model to explain heterogeneous plastic deformation, large lattice rotation within shear bands and the inhomogeneous distribution of dislocations when a sample is subjected to stress. In this method, the continuum mechanical behavior of the material is specified by finite strain crystal plasticity, while the self-hardening and dislocation microstructure evolution within each slip system is defined by a local dislocation density model consistent with global deformation. Since the dislocation model treats dislocations as defect density and interaction among dislocation is considered, this method is computationally more efficient and the simulation of the evolution of microstructure is feasible. The interaction between each slip system is modelled on the basis of experimental measurements. Single crystal mechanical behavior and dislocation microstructure can be studied directly with this model. The model is also extended to simulate plastic deformation in polycrystlas, and to compare to experiments.

In this chapter, the algorithm for single crystal plasticity , solution approach and the method to couple single crystal plasticity will be discussed. Since the

development of a dislocation density based model is a relatively independent process and the different formulation and solution approach were used, the details of the dislocation density based model will be discussed in chapter 5.

4.2 Objectives

These objectives of the present modeling are:

1. Single and Polycrystal plasticity formulation and implementation using finite element method with developing users material subroutine UMAT in ABAQUS.

2. Further development of Ghoniem-Matthews-Amodels (GMA) [25] dislocation density based material model to define the strain hardening in each slip system.

3. Coupling crystal plasticity with dislocation density based material model within the finite element framework to study heterogeneous plasticity behavior and dislocation microstructure evolution during plastic deformation in materials.

These three objective will be fulfilled within this chapter and next chapter.

4.3 $3D$ Crystal Plasticity Modelling with 2 and 12 Slip Systems

The material simulated is pure copper and assumed to be elastically isotropic. The material parameters are [80]:

- Young's modulus is : 130 Gpa
- Poisson's ratio is : 0.32.

Since we are working on material modelling in this chapter rather than single or polycrystal structure analysis, we are modelling the mechanical behavior and microstructure evolution at a material point. $3D$ crystal plasticity with 2 or 12 slip systems means that at an arbitrary material point, all kinematics and constitutive behavior are specified in 3 dimensions, material stiffness matrix is a fourth order tensor, and stress and strain are second order tensor. To make it clearer, figure 4.2 or figure 4.3 show that at a material point there are 2 slip systems or 12 slip system in the modelling, rather than describe a single crystal structure.

Convention of crystallographic orientation:

- For crystal plasticity model with 2 slip system: crystallographic orientation refers to angle θ between the normal $m : (110)$ of slip plane and the horizontal axis as shown in figure 4.1. Lattice rotation refers to the net change of this angle caused by rotation.
- For crystal plasticity model with 12 slip system, since this structure is an fcc crystal structure. The initial crystallographic orientation is defined with three angles, θ_1, θ_2, θ_3 to track its evolution. These three angles are defined as the rotation angle of [100], [010] and [001], respectively.

4.3.1 Modelling of Single Crystal Plasticity with 2 Slip Systems

2 slip planes and slip directions are defined as in figure 4.2. Since there are two slip systems defined at a material point, two yields functions are needed for both

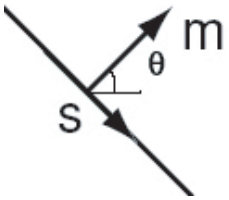

Figure 4.1: The convention of crystallographic orientation θ used in this model

of these two slip systems to be activated at the same increment step.

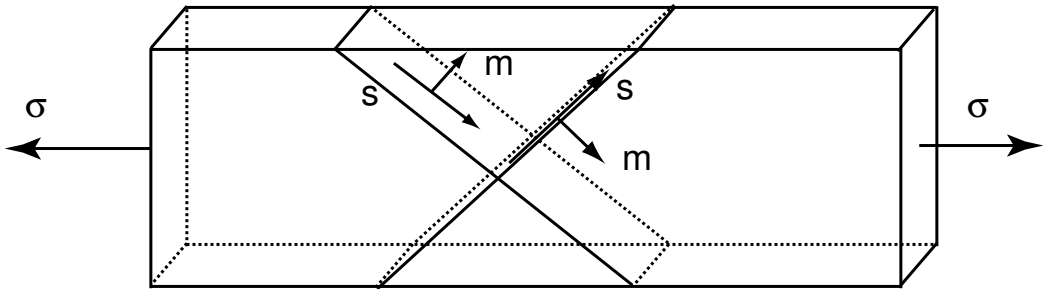

Figure 4.2: Slip planes and slip directions in single crystal with two slip systems

Table 4.1: Slip directions s^α and slip planes m^α for the 2 slip system

α	s^α	m^α
1	$[1\bar{1}0]$	(110)
2	$[110]$	$(1\bar{1}0)$

4.3.2 Modelling Single Crystal Plasticity with 12 Slip Systems

4 slip planes and 3 slip directions on each slip plane are defined as in figure 4.3. This combination gives 12 slip systems.

These two material models will be applied to study the deformation of single and Polycrystalline copper. Detailed information of geometrical shape, boundary

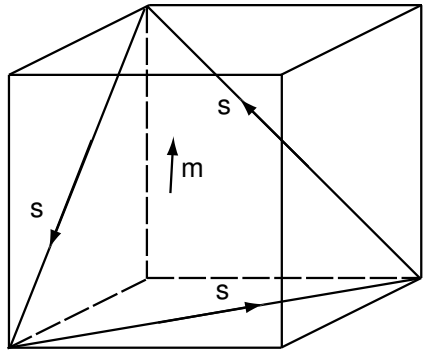

Figure 4.3: Slip planes and slip directions in $3D$ single crystal

Table 4.2: Slip directions s^α and slip planes m^α for 12 slip systems

α	s^α	m^α	α	s^α	m^α	α	s^α	m^α
1	$[01\bar{1}]$	(111)	5	$[101]$	$(\bar{1}11)$	9	$[\bar{1}\bar{1}0]$	$(\bar{1}1\bar{1})$
2	$[\bar{1}01]$	(111)	6	$[\bar{1}\bar{1}0]$	$(\bar{1}11)$	10	$[011]$	$(11\bar{1})$
3	$[1\bar{1}0]$	(111)	7	$[011]$	$(\bar{1}1\bar{1})$	11	$[1\bar{1}0]$	$(11\bar{1})$
4	$[01\bar{1}]$	$(\bar{1}11)$	8	$[10\bar{1}]$	$(\bar{1}1\bar{1})$	12	$[101]$	$(11\bar{1})$

conditions will be discussed in each specified case in chapter 6

4.4 Algorithm and Solution Approach for $3D$ Crystal Plasticity Model

4.4.1 Algorithm

Since kinematics of single crystal plasticity deformation was built conceptually based on finite strain crystal plasticity [8] as introduced in chapter 3, only the algorithm of solving crystal plasticity with finite element method and solution approach to solve for the yield function and obtain the true solution and updates of state variables are discussed here.

Assume $\mathcal{D} \in R^3$ be the body of interest and $\mathbf{u} : \mathcal{D} \to R^3$ is a given displacement field. The strain tensor is $\varepsilon = \frac{1}{2}(\mathbf{F}^T\mathbf{F} - \mathbf{I})$. Total strain is split into plastic and elastic strain.

$$\varepsilon = \varepsilon^e + \varepsilon^p \tag{4.1}$$

The elastic energy is:

$$\mathbf{E}(\varepsilon^e) = \frac{1}{2}\varepsilon^e : \mathcal{C}^e : \varepsilon^e \tag{4.2}$$

and the stress is given by:

$$\sigma = \frac{\partial E(\varepsilon^e)}{\partial \varepsilon^e} = \mathcal{C}^e : \varepsilon^e \tag{4.3}$$

where C^e is a fourth-order tensor of elastic moduli as:

$$\mathcal{C}^e = \mathcal{C}^{eijkl} e_i \otimes e_j \otimes e_k \otimes e_l \tag{4.4}$$

Assumption:

In single crystals, plastic deformation takes place on certain crystal planes and

along certain directions. When a single crystal is subjected to an external stress, the projection of the stress tensor along the specified slip direction on the specified slip plane is called the Schmid stress. When the Schmid stress is higher than the resistance on that slip system, plastic deformation will take place. If $\Delta\sigma$ is external stress increment at step, the Schimd stress increment $\Delta\tau$ on a specified slip system is defined by Eq. 4.5:

$$\mathbf{\Delta}\tau = \mathbf{\Delta}\sigma : \mathbf{P}^{\alpha} \tag{4.5}$$

where P^{α} is the symmetric space spanned by the slip direction s^{α} and slip plane normal m^{α}. Both s^{α} and m^{α} are subjected to the coordinate transform operations defined by Eq. 3.37 and 3.38 at the beginning of each incremental step, respectively. Then P^{α} is updated by the operation defined by:

$$P^{\alpha} = \frac{1}{2}(s^{\alpha} \otimes m^{\alpha} + m^{\alpha} \otimes s^{\alpha}) \tag{4.6}$$

An algorithm is applied to compute single crystal plasticity as follows:

1. Trial strain:

$$\Delta\varepsilon_{n+1} = \Delta\varepsilon^{e}_{n+1} + \Delta\varepsilon^{p}_{n+1} \tag{4.7}$$

2. Macro stress:

$$\Delta\sigma_{n+1} = C^{e} : \Delta\varepsilon_{n+1} \tag{4.8}$$

3. Schmid stress:

$$\Delta\tau^{\alpha}_{n+1} = \Delta\sigma_{n+1} : P^{\alpha}_{n} \tag{4.9}$$

4. Yield function:

$$\Phi^{\alpha}_{n+1} = (\tau^{\alpha}_{n} + \Delta\tau^{\alpha}_{n+1}) - \tau^{\alpha}_{0} - g^{\alpha}_{n+1} \tag{4.10}$$

5. Flow rule:

$$\Delta\varepsilon^{p}_{n+1} = \sum_{\alpha\in A} \gamma^{\alpha} \frac{\tau^{\alpha}_{n}}{|\tau^{\alpha}_{n}|} P^{\alpha}_{n} \tag{4.11}$$

where A mean the activated slip system.

6. Hardening law:

$$g^{\alpha}_{n+1} = g^{\alpha}_{n} + \sum_{\beta\in A} h^{\alpha\beta}_{n} \gamma^{\beta} \tag{4.12}$$

Where, $h^{\alpha\alpha}_{n}$ is self-hardening rate for each slip system caused by interaction of dislocations within the same slip system. It is derived directly from the tangent stiffness calculated from the dislocation density based model. $h^{\alpha\alpha}_{n}$ is the known value of of tangent at the end of step n.

$$h^{\alpha\alpha}_{n} = \frac{\Delta\sigma^{\alpha}_{n}}{\Delta\varepsilon^{\alpha}_{n}} \tag{4.13}$$

$$h^{\alpha\beta}_{n} = h^{\alpha\alpha}_{n}[q + (1-q)\delta^{\alpha\beta}] \qquad \alpha \neq \beta \tag{4.14}$$

$h^{\alpha\beta}_{n}$ when $\alpha \neq \beta$ is latent hardening caused by interaction of dislocation between different slip system. $q = 1.4$ is defined based on experimental results [8].

7. Kuhn-Tucker and consistency condition:

$$\gamma^{\alpha} \geq 0 \tag{4.15}$$

$$\Phi^{\alpha}_{n+1} \leq 0 \tag{4.16}$$

$$\gamma^{\alpha}\Phi^{\alpha}_{n+1} = 0 \tag{4.17}$$

Substitute above equations into equation 4.10 and then solve for the yield function of each slip system:

$$\Phi^{\alpha}_{n+1} = P^{\alpha}_{n} : C^{e} : (\varepsilon^{e}_{n} + \Delta\varepsilon_{n+1}) - g^{\alpha}_{n} - \tau^{\alpha}_{0} - \sum_{\beta \in A} (P^{\alpha}_{n} : C^{e} : P^{\beta}_{n} + h^{\alpha\beta}_{n})\gamma^{\beta} = 0 \quad (4.18)$$

To solve the yield functions of the total system, we solve the following linearized equations simultaneously.

$$\sum_{\beta \in A} (P^{\alpha}_{n} : C^{e} : P^{\beta}_{n} + h^{\alpha\beta}_{n})\gamma^{\beta} = P^{\alpha}_{n} : C^{e} : (\varepsilon^{e}_{n} + \Delta\varepsilon_{n+1}) - g^{\alpha}_{n} - \tau^{\alpha}_{0} \qquad (4.19)$$

The left hand side is a 12×12 matrix for $3D$ crystal plasticity with 12 slip systems or a 2×2 matrix for the same modelling but with 2 slip systems. Solve for γ^{β} under the constraints of Khun-Tucker conditions and consistency conditions.

4.4.2 Solution Approach

4.4.2.1 Forward Euler Method for the Plastic Increment

Many algorithms for solving isotropic plasticity as an internal iteration for strain-driven finite element method were developed, such as the return mapping method of Wilkins [79], and the cutting plane method of Simo and Ortiz [63]. Both methods are implicit, and they obtain the elastic strain by iteration. Convergence of these methods is unconditional. As we know, isotropic plasticity only has one yield surface which is a sphere with the radius of the yield stress in the deviatoric stress space. However, the yield surface of the single-crystal plasticity is multi-surface. It's extremely hard to adopt these methods to solve this multi-nonlinear yield functions, as shown by Luenberger [43], Simo *et al.* [64], Cuitino and Ortiz [18], Ortiz and Stainier [49] and Miehe [47]. The rate-independent case is considered here and the algorithm for internal iteration to determine

the activated slip system developed by Cuitino and Ortiz [18] and Miehe [47]is conceptually followed.

The method we used here is a forward Euler integration method with very small incremental steps to solve for plastic increments on each slip system. Assuming all variables to be known at step n, we solve for the plastic increment on each slip system at step $n+1$.

The initial values are $\varepsilon^p = 0$, $A = 0$, $g^\alpha = \tau_0$ before yield occurs.

The applied $\Delta\varepsilon_{n+1}$ is total trial strain in step $n+1$ and is treated as a pure elastic strain increment in this step. The trial stress and trial shear stress on each slip system are computed as defined in Eq. 4.9. We then substitute these stresses in the yield functions definde by Eq. 4.10. When all yield functions are less than zero, this step is purely elastic, then we perform the global momentum balance until it is satisfied. Another increment is then applied.

If any yield function 4.10 is violated, we solve the equation system 4.19 under the constraints $\gamma^\alpha > 0, \quad \Phi_{n+1} \leq 0 \quad and \quad \gamma^\alpha \Phi^\alpha_{n+1} = 0$, as described in the next section.

4.4.2.2 Determination of Activated Slip Systems

If any $\gamma^\alpha < 0$, the system with the minimum load is dropped from the active working set, and the remaining equations are solved again until all $\gamma^\alpha > 0$.

After obtaining the solution with all $\gamma^\alpha > 0, \alpha \in A$, The other condition $\Phi^\alpha \leq 0, \alpha \in A$ is also checked. If any yield function $\Phi^\alpha > 0, \quad \alpha \in A$, we remove this function and the maximum loaded system which has not been previously activated will be put into the yield equations and the system is solved.

Internal iterations are performed until all conditions are satisfied.

4.4.2.3 Numerical Algorithm for Ill-Conditioned and Singular Local Jacobian

To find the solution $x \in R^n$ of $Ax = b$, where $A \in R^{n\times n}$ and $b \in R^n$ are known, this problem has a solution only if $b \in R(A)$, and it is unique if and only if $N(A) = 0$, wher $N(A)$ is the determinant of the matrix.

However, due to the typical multiplicity of slip systems in a single crystal with various crystal orientations and the complicated loading conditions, the matrix A could be singular. For the linear equation system of multi-yield functions for rate-independent crystal plasticity under the assumption that $b \in R(A)$, there should be a solution. Under this condition, $Ax = b$ has a set of solution x, but it is not unique. Here, a powerful singular value decomposition method is employed.

A singular value decomposition (SVD) of an $n \times n$ real matrix A is a factorization of the the form [54].

$$A = U_1 D U_2^T \tag{4.20}$$

where

$$U_1^T U_1 = U_2^T U_2 = I \tag{4.21}$$

$$D = diag(d_1, d_2, ..., d_n) \qquad where, \quad d_1 \geq d_2 \geq ... \geq d_n \geq 0 \tag{4.22}$$

the columns of U_1 are orthonormalized eigenvectors of AA^T, and columns of U_2 are the orthonormalized eigenvectors of $A^T A$. The diagonal elements of D are the non-negative square roots of eigenvalues of AA^T and $A^T A$, and they are named the singular values of A. The singular value decomposition is unique.

By doing singular value decomposition, the rank r of matrix A is the number of non-zero singular values. If the $rank(A) = r$, $d_{r+1} = d_{r+2} = ... = d_n = 0$.

If $A = U_1 D U_2^T$ is the singular value decomposition of A, the pseudoinverse of A is defined by:

$$\begin{aligned} A^+ &:= U_2 D^+ U_1^T && (4.23) \\ where \quad D^+ &= diag(d_1^+, d_2^+, ..., d_n^+) && (4.24) \\ d_i^+ &= \frac{1}{d_i} \qquad for \quad d_i > 0 && (4.25) \\ &= 0 \quad for \quad d_i = 0 && (4.26) \end{aligned}$$

We can see that, if A is square and non-singular, all the singular values are non-zero. The pseudoinverse is the same as the inverse when A is the non-singular.

Assume that $b \in R(A)$ is the given vector, and A in the equations system $Ax = b$ is singular. As we discussed, the solution to this system is not unique. however, solution can be obtained by the following method is unique.

$$x^+ = A^+ b \tag{4.27}$$

This solution has the important characteristics among all the solutions x which satisfy $Ax = b$.

$$\|x^+\| = (x^T x)^{\frac{1}{2}} = min \tag{4.28}$$

This solution is chosen as the solution for the yield functions based on the principle of minimum dissipation of plastic energy.

4.4.3 Update of Elastic and Plastic Strain Variables

When all γ^α are obtained, the plastic strain increment in this step is:

$$\Delta\varepsilon^p_{n+1} = \sum_{\alpha\in A} \gamma^\alpha \frac{\tau^\alpha_n}{|\tau^\alpha_n|} P^\alpha_n \tag{4.29}$$

The plastic strain, elastic strain, strain hardening and stress are updated as defined by:

$$\begin{aligned}
\varepsilon^p_{n+1} &= \varepsilon^p_n + \sum_{\alpha\in A} \gamma^\alpha \frac{\tau^\alpha_n}{|\tau^\alpha_n|} P^\alpha_n && (4.30)\\
\varepsilon^e_{n+1} &= \varepsilon^{trial}_{n+1} - \sum_{\alpha\in A} \gamma^\alpha \frac{\tau^\alpha_n}{|\tau^\alpha_n|} P^\alpha_n && (4.31)\\
g^\alpha_{n+1} &= g^\alpha_n + \sum_{\beta\in A} h^{\alpha\beta}_n \gamma^\beta && (4.32)\\
\sigma_{n+1} &= \sigma_n + \mathcal{C}^e : (\Delta\varepsilon_{n+1} - \Delta\varepsilon^p_{n+1}) && (4.33)
\end{aligned}$$

4.4.4 Update of the Elasto-plastic Tangent Moduli

The stress is obtained by plugging equation 4.7 into 4.8 to get:

$$\Delta\sigma = \mathcal{C}^e : \Delta\varepsilon - \sum_{\alpha\in A} \gamma^\alpha (\mathcal{C}^e : P^\alpha) \tag{4.34}$$

The consistency equations give:

$$\frac{\partial\gamma^\alpha}{\partial\Delta\varepsilon} = \mathcal{D}^{\alpha\beta-1}(P^\beta : \mathcal{C}^e) \tag{4.35}$$

Where, $\mathcal{D}^{\alpha\beta} = P^\alpha : \mathcal{C}^e : P^\beta + h^{\alpha\beta}$

Based on this result, the stress increment is:

$$\Delta\sigma = \mathcal{C}^{ep} : \Delta\varepsilon \tag{4.36}$$

Then, elasto-plastic moduli is:

$$\mathcal{C}^{ep} = \mathcal{C}^{e} - \sum_{\alpha \in A} \sum_{\beta \in A} \mathcal{D}^{\alpha\beta-1} (\mathcal{C}^{e} : P^{\alpha}) \otimes (P^{\beta} : \mathcal{C}^{e}) \tag{4.37}$$

In this problem, the elastic property of the crystal is assumed to be isotropic, and the elasto-plastic moduli can be also expressed as:

$$\mathcal{C}^{ep} = \kappa \mathbf{1} \otimes \mathbf{1} + 2\mu(\mathbf{I} - \frac{1}{3}\mathbf{1} \otimes \mathbf{1}) - 4\mu^2 \sum_{\alpha \in A} \sum_{\beta \in A} \mathcal{D}^{\alpha\beta-1} P^{\alpha} \otimes P^{\beta} \tag{4.38}$$

Where, $\mathbf{1}$ is second order identity tensor, and $\mathbf{I}$ is fourth order identity tensor.

After updating all values, global momentum conservation is tested. If it is satisfied, the next incremental step is carried out. If not, another trial displacement is applied and a new internal iteration is performed until global momentum equilibrium is reached within a predefined tolerance.

4.5 Method to Couple Crystal Plasticity with Dislocation Density Based Material Behavior

4.5.1 Introduction

The general idea of coupling crystal plasticity with a dislocation density based model is to use finite strain crystal plasticity method to define the material's continuum mechanical behavior, and use a concurrent dislocation density based model to define self-hardening effects on each slip system. The finite element software ABAQUS is employed as a tool to build the geometric shape of grains (single crystal or polycrystal) and to perform the FEM solution. ABAQUS provides a special interface, called user subroutine UMAT, which allows the user to define the mechanical behavior of a material and to interface with any externally

defined programs.

The user subroutine UMAT has the following main functions which can be coded with Fortran or C++ [36]

1. It can be used to define the mechanical constitutive behavior of a material;
2. It can be used with any procedure that includes mechanical behavior;
3. It can use solution-dependent state variables;
4. It must update the stresses and solution-dependent state variables to their values at the end of the increment for which it is called;
5. It must provide the material Jacobian matrix, $\partial\sigma/\partial\varepsilon$, for the mechanical constitutive model;

4.5.2 Coupling Method

The flow charts shown in figure 4.4 and figure 4.5 show that how UMAT interface with the finite element code and how the dislocation-based material model is coupled with crystal plasticity .

Figure 4.4 shows the general procedure for the finite element method. At step n an displacement increment is applied and first the external iteration is started. ABAQUS uses the stiffness tangent of the user defined material model at every integration point to calculate the element stiffness $\mathbf{K^{el}}$ and global stiffness matrix $\mathbf{K}$. At the beginning of each global increment step, UMAT is called for computing the material jacobian matrix D to obtain $\mathbf{K^{el}}$ and assemble $\mathbf{K}$. Elastic, plastic strain, stress and material jacobian are determined by solving for the yield functions with internal iterations. When the yield functions are solved and all aforementioned four unknown states are determined by UMAT, global

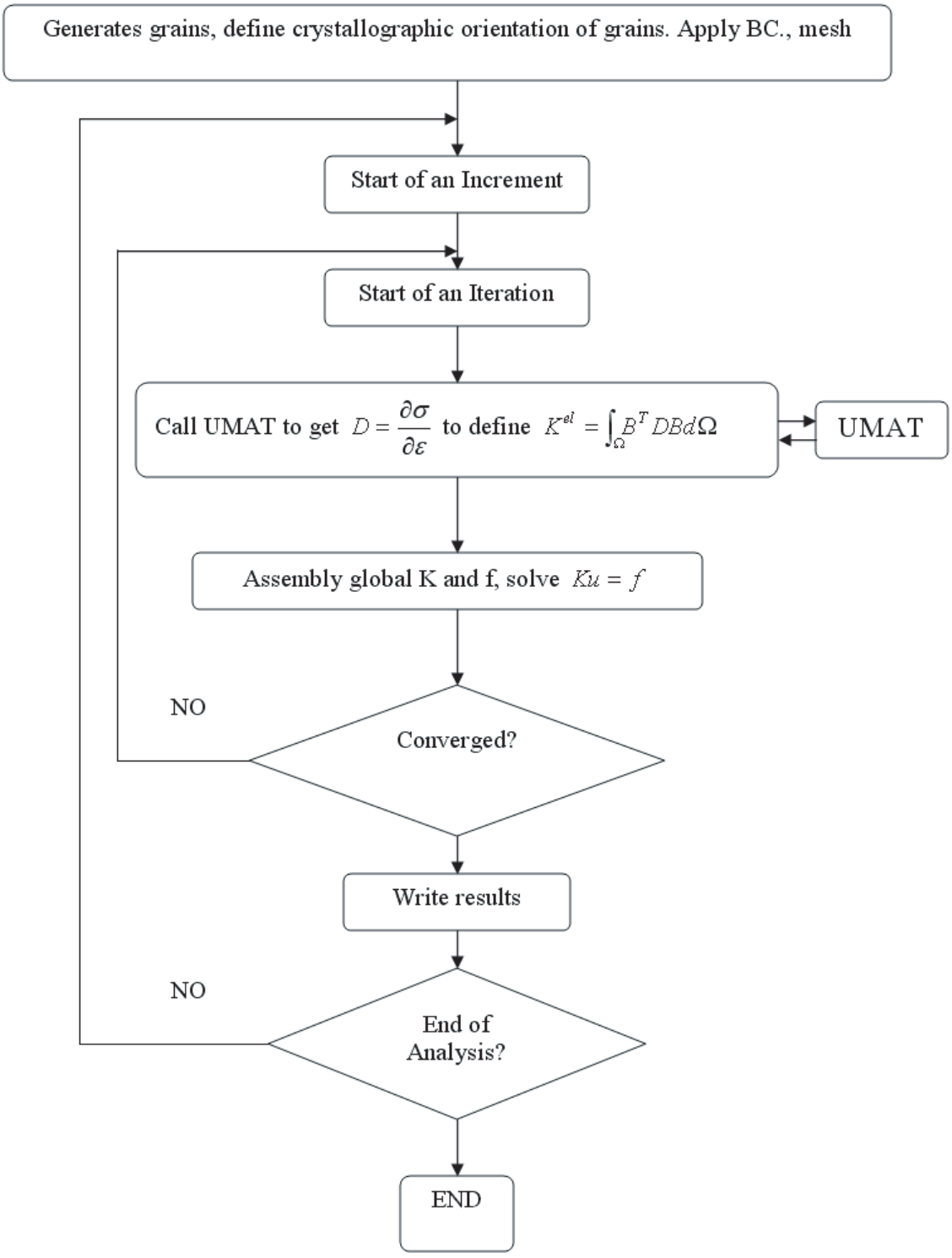

Figure 4.4: Flow chart of finite element method to solve crystal plasticity modelled with UMAT

momentum balance is tested based on this solution. If the global momentum equilibrium is reached, a next increment step will be applied. If the global force equilibrium is not reached within the given tolerance, another trial iteration will be given and UMAT will be called again to repeat the process as mentioned before until the global momentum equilibrium is reached.

Figure 4.5 shows a flow-chart for coupling the dislocation-based constitutive model with crystal plasticity. When it is determined that at least one slip system is activated, the dislocation-based model is called. The resultant Schmid stress on that slip system will be used as the applied stress in Eq. 5.8 to calculate the effective stress on that slip system. This effective stress is plugged into Eq. 5.13 in the same dislocation model to calculate dislocation glide velocity. Then the dislocation glide velocity derived from Eq. 5.13 is substituted into ODE 5.49 and 5.51, and six coupled ordinary differential equations are solved simultaneously with the forward Euler method. The stress-strain relation computed from this model is used in UMAT to define self-hardening and to compute the plastic strain increment within each slip system by solving for the yield functions. Then elastic, plastic strain and stress in step $n + 1$ are thus computed. At the same time, microstructure evolution is computed from these six ODEs is fed back to UMAT to record the information of microstructure at this integration point. A global momentum balance is then tested. If this iteration converges, the program leaves UMAT and applies another increment and do step $n + 2$. If not, another trial strain is applied and the Schmid stress is calculated to determine if a slip system is activated. If at least one slip system is activated, the dislocation-based model is called and the aforementioned procedure is performed until convergence is reached.

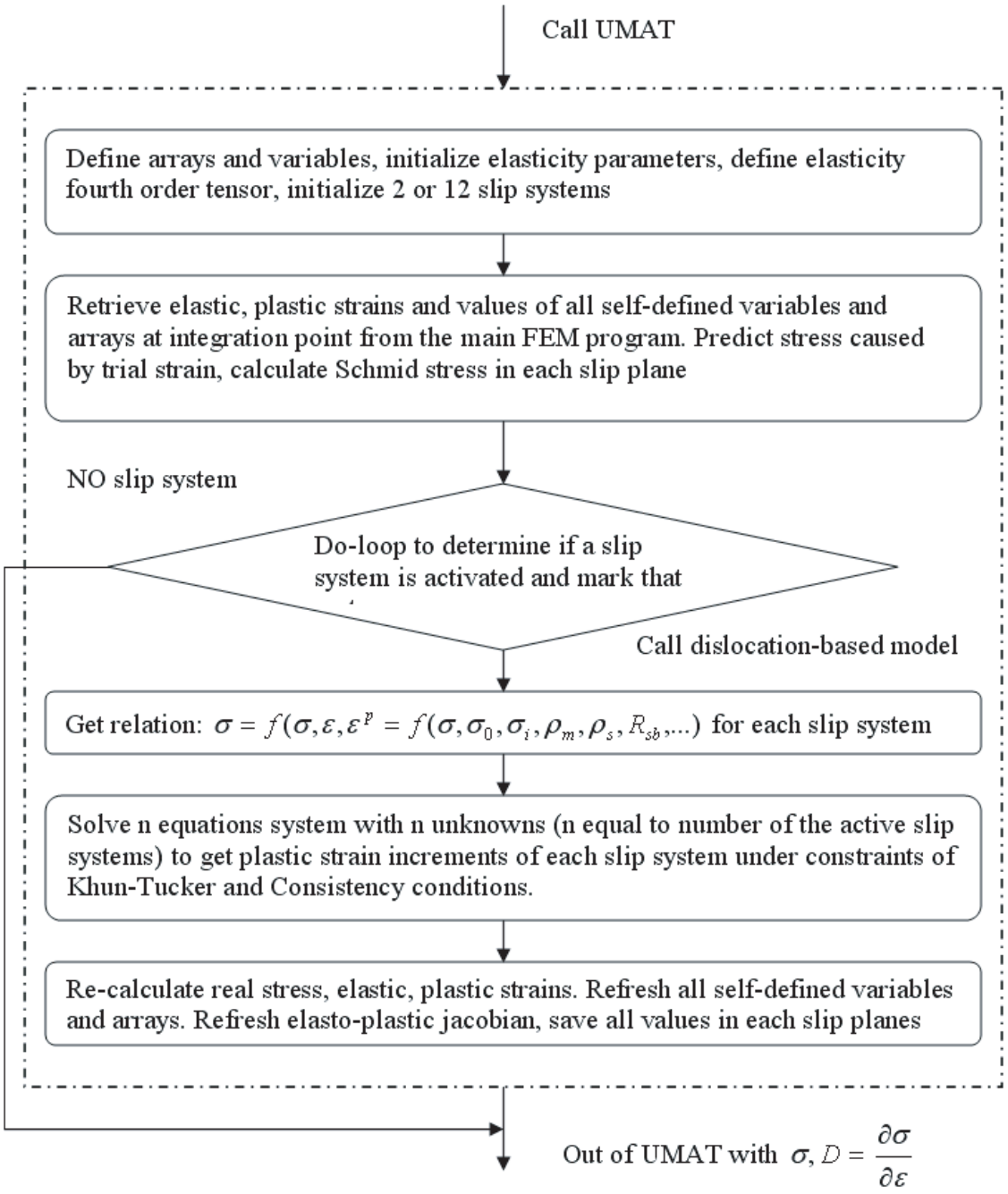

Figure 4.5: Flow chart of UMAT coupling dislocation-based model with crystal plasticity model

CHAPTER 5

Dislocation Density Based Modelling of Self-Hardening

In this chapter, a dislocation density based materials model developed by Ghoniem *et al.* [25] will be further extended to define strain hardening within slip system of single crystal. The strain hardening effect computed from this model will be employed to specify the self-hardening effects directly and Latent hardening are determined from self-hardening via a constant coefficient established experimentally. These two hardening effects define the diagonal and off-diagonal terms in the hardening matrix of crystal plasticity model, respectively. The dislocation density based model makes it possible to accurately capture the physical behaviors of strain hardening at the microscale. When it is coupled with crystal plasticity, macroscale heterogeneous plasticity and microscale dislocation evolution can be simulated at the same time within the main frameworks of finite element method.

The model by Prinz *et al.* [55] was formulated based on defining the relationship between the resistance τ and plastic slip. The plastic strain is solved based on the solution of the resistance. The model by Lagneborg *et al.* [40], is based on formulating the dislocation distribution frequency function $\Phi(l)$. The evolutionary equations of dislocation density is computed by integration of the frequency function. The research work by Nabarro [50] on the diffusion creep and

the work by Gittus[29] on the dislocation creep have all contributed to progress on the constitutive models of plastic deformation..

5.1 An extension of Ghoniem-Matthews-Amodeo's (GMA) Model

Ghoniem et al [25] summarized a number of models (Takeuchi et al[66], Langdon[41], Challenger et al[15], Michel et al[46], and Cuddy[17]) on the investigations of subgrain and developed this model. In this model, six ordinary partial differential equations are built to study evolution of mobile, static, boundary dislocation and dislocation subgrain, as shown in figure5.1, and strain stress behavior of the material is computed at the same time.

5.1.1 Model Assumptions

Here, assumptions made by Ghoniem's model are listed before discussing the details of the modelling.

- Dislocation pileups and debris caused by cold works are not observed.
- Dislocations form a polygonal network which is evolved at high temperature and low stress. This microstructure is called subgrain.
- The Radius of the subgrains is inversely proportional to the applied stress.
- The dislocation density within the subgrains are lower than boundaries, and increases proportionally to the square of the applied stress.
- In materials with lower stacking fault energy, subgrains may be formed only at higher temperatures.

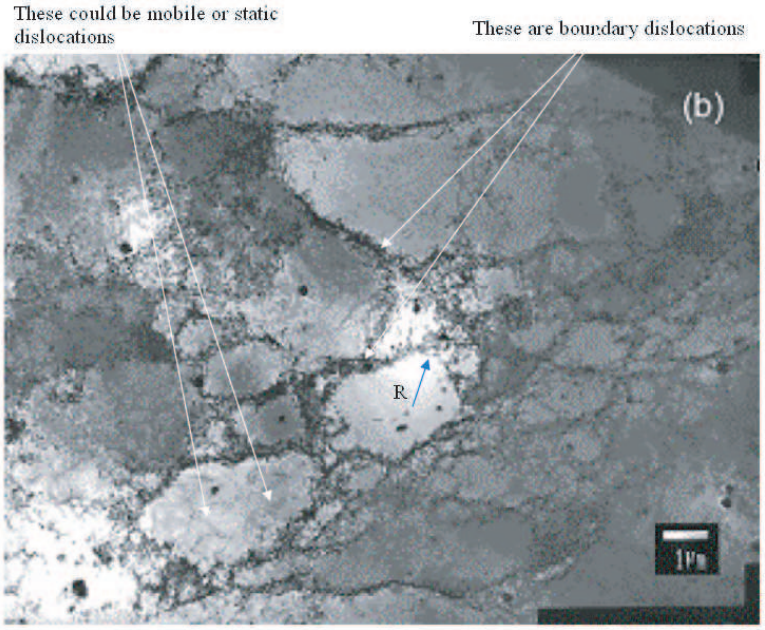

Figure 5.1: An experimental observation done by Dr. Singh *et al* [65]. Dislocation subgrain structure can be observed and boundary dislocations are very dense within subgrain boundary. Mobile and static dislocations are inside subgrain as pointed by arrows. However, whether the pointed dislocation is mobile or static cannot be distinguished from this photo.

- The misorientation within subgrain boundaries is subjected to a long transient which saturated only after tens of percent strain, but this value is not related to the applied stress and temperature.

Several dislocation processes proposed by Gittus[26] and Sandström[59, 58] are also be summarized here.

- Multiplications of mobile dislocations within the subgrains.
- Annihilation of mobile dislocations caused by the interactions among them within the subgrains.

- Annihilation of dislocations at the subgrain boundaries.
- Absorption of dislocations by the subgrain boundaries.
- Emissions of dislocations from the subgrain boundaries.
- Nucleation of new subgrains from dislocations within cells.
- Growth of subgrains by coalescence to reduce subgrain boundary surface energy.

5.1.2 Dislocation Multiplication and Immobilization

Orowan equation is adopted to define the relationship between strain rate and dislocation density in Ghoniem's model [25].

$$d\varepsilon^p/dt = b\rho_m v_g \tag{5.1}$$

ε^p is the creep or plastic strain. ρ_m is the mobile dislocation density. v_g is the glide velocity, and b is the Burger's vector. The glide process is assumed to be easy, and climb of dislocation has no contribution to strain rate. To model the self-hardening effect within slip system, only one slip system is considered.

To formulate a rate equation for mobile dislocation, the rate of dislocation production and annihilation must be defined. The subgrains provides a source and also acts as a barriers for mobile dislocations. The rate of the mobile dislocation is generated within the subgrains is specified by the frequency of the dislocation produciton multiplied by the number of dislocation produced. It is defined in by Eq. 5.2.

$$\dot{\rho_m} = \rho_m^{3/2} v_g \tag{5.2}$$

The frequency of production is $\rho_m^{1/2} v_g$, where $\rho_m^{1/2}$ is the reciprocal of the mean free path of the mobile dislocations. The density of source in subgrains can be defined as $\frac{1}{2} h^2 R_{sb}$, where h is the dislocation spacing within the subgrains, and R_{sb} is the radius of subgrains. The dislocation spacing within the subgrain boundary h, is defined by Eq. 5.3, where ρ_s and ρ_b are density of static and boundary dislocations.

$$h = 1/(\rho_s + \rho_b) R_{sb} \tag{5.3}$$

two rate equations for mobile and static dislocation populations are defined by Eq. 5.4 and 5.5.

$$\dot{\rho_m} = \beta \rho_s R_{sb} v_g / h^2 - \rho_m v_g / 2 R_{sb} \tag{5.4}$$

$$\dot{\rho_s} = \rho_m v_g / 2 R_{sb} \tag{5.5}$$

where β is a density factor.

5.1.3 Internal Stress

In the GMA model[25], the internal stress is caused by any opposition to dislocation motions, and this opposition can be caused by three sources. The first possible source is dislocations or precipitates that oppose dislocation motions. The internal stress that mobile dislocations must overcome to move is $\mu b / 2\pi\lambda$, where λ is the effective obstacle spacing, and μ is the shear modulus. under the situation that both precipitate and dislocation obstacles are present, the effective spacing λ between obstacle is defined as Eq. 5.6.

$$\lambda = 1/(1/\lambda_d + 1/\lambda_p) \tag{5.6}$$

Where, λ_d is the inter-dislocation spacing and defined by $\lambda_d = 1/\rho_m^{1/2}$. λ_p is the inter-precipitates spacing defined by $\lambda_p = 1/(N_p r_p)^{1/2}$, where N_p is the volume concentration of precipitates, and r_p is the mean radius.

The second source of opposition are the dislocations that have not been neutralized their long range stress fields since these dislocations have not moved into their lowest energy configuration. The mobile dislocations could be accelerated through this field or dragged by it depending on the sign of these un-neutralized stress fields. The sub-boundary dislocations themselves do not contribute to the internal stress out of a distance greater than the average dislocation distance within the subgrains[24]. The main effect from static dislocation to internal stress is defined as $\xi\mu b\rho_s^{1/2}$. The long range internal stress σ_i is defined by Eq. 5.7.

$$\sigma_i = \mu b/2\pi\lambda + \zeta\mu b\rho_s^{1/2} \tag{5.7}$$

The third source of contribution to internal stress is caused by the friction resistance to glide from over-sized solutes. For the well-annealed materials without hardening precipitates and heat treatment, this stress can be defined as the initial flow stress, σ_0. The total effective stress is defined by Eq. 5.8.

$$\sigma_e = \sigma_a - \sigma_i - \sigma_0 \tag{5.8}$$

where σ_a is the applied stress. When coupling this dislocation density based model with crystal plasticity model, the applied stress in Eq. 5.8 is defined by Schmid stress in this slip system. Long range stress and initial flow stress are material internal properties, defined in this model. Later on, the effective stress defined by Eq. 5.8 will be plugged in to Eq. 5.13 to calculate dislocation glide velocity.

5.1.4 Dislocation Velocity

In the GMA model[25], the dislocation velocity does not affect the steady state creep strain rate significantly. However, the dependency of velocity on stress affects relationship between stress and dislocation density and strain rate. Assuming that dislocations do not form sinks for the solute, under low stresses, the gliding velocity of dislocation is defined as in Eq. 5.9[67, 16]:

$$v_g = D_a kTb\sigma_e/[c_0(\beta^*)ln(R/r)] \tag{5.9}$$

where σ_e is the effective stress, c_0 is the uniform volume concentration of the solute, D_a is the solute diffusion coefficient, R is the outer cutoff radius defined as $R = \rho_m^{-1/2}$, and r is the inner cutoff radius defined as $r = \beta^*/kT$. The value of β^* is defined by Eq. 5.10 [33].

$$\beta^* = (\mu b/3\pi)[(1+\nu)/(1-\nu)](v_s - v_a) \tag{5.10}$$

where ν is the Poisson's ration, v_s is the solute atomic volume, and v_a is the volume of matrix atoms .

When solute atoms are trapped at the core of the dislocations, the velocity is defined as Eq. 5.11 [33]:

$$v_g \approx 2bv_d exp(-2W_a/kT)sinh(\sigma_e b^2 l_a/kT) \tag{5.11}$$

where v_d is the dislocation vibrational frequency, W_a is the activation free energy for core diffusion of the solute, and l_a is the spacing of the solute atoms in the core.

The dislocation glide velocity can also be defined by another equation as Eq. 5.12

$$v_g = a_1 exp(-W_g/kT)\sigma_e\Omega/kT \tag{5.12}$$

where a_1 and W_g are parameters need to be fitted, and Ω is the atomic volume.

If the effect of cutting of the obstacles like coherent or semi-coherent precipitates is considered, glide velocity is defined as Eq. 5.13

$$v_g = v_d\lambda sinh(\sigma_e b^2\lambda/2kT)exp(-U_g/kT) \tag{5.13}$$

U_g is the activation energy for the process, which is approximately twice the jog formation energy for the dislocation intersection. The effective stress σ_e is defined by Eq. 5.8.

5.1.5 Climb and Recovery

Climb recovery is a process that, for both mobile and static dislocation, climbing together of dislocation dipole over time. During climbing of dislocation through the subgrain wall, the annihilation is not considered. The effective stress exerted by dislocation dipoles on each other can be defined as Eq. 5.14, where s is the separation distance between the dipoles.

$$\sigma_c = \mu b/2\pi(1-\nu)s \tag{5.14}$$

The vacancy concentration close to the dislocations c^c_{vd} will be affected by the energy field generated by dislocation. If the thermal equilibrium vacancy concentration is c^c_v, then c^c_{vd} can be defined as Eq. 5.15.

$$c_{vd}^{c} = c^{c} exp(\pm \frac{\sigma_c \Omega}{kT}) \simeq c^{c}(1 \pm \frac{\sigma_c \Omega}{kT}) \tag{5.15}$$

To make it easier to consider the inclusion of irradiation effect. The net flow of vacancies into dislocations is defined as Eq. 5.16

$$\frac{dq_d}{dt} = k_{id}^2 D_i c_i - k_{vd}^2 D_v c_v + k_{vd}^2 D_v c_{vd} \tag{5.16}$$

k_{id}^2, D_i, and c_i are the dislocation sink strength for interstitial, interstitial diffusion coefficient, and the interstitial bulk concentration. k_{vd}^2, D_v, and c_v are the corresponding terms for vacancies. Under irradiation, the interstitial and vacancy concentration are defined as Eq. 5.17 and 5.18.

$$\frac{\partial c_i}{\partial t} = K + k_i^2 D_i ci - \alpha c_i cv \tag{5.17}$$

$$\frac{\partial c_v}{\partial t} = K + k_v^2 D_v cv - \alpha c_i cv \tag{5.18}$$

where K is the rate of production of Frenkel pairs, k_i^2 and k_v^2 are the total effect of the sink strength from all the potential sinks for interstitial and vacancies, Kv^e is the sum of the vacancy emission rate for all the sinks, α is the rate constant specifying the recombination of interstitial and vacancies. According to Rauh and Bulllogh[56], the sink strength is defined as Eq. 5.19

$$k_{\alpha N}^2 = -\frac{\pi \rho_N}{ln[(1/2)e^{\gamma}(k_\alpha L_\alpha)]} \simeq -\frac{2\pi\rho N}{ln(k_\alpha L_\alpha)} \tag{5.19}$$

where the subscript α refers to interstitial or vacancy, the subscript N refers to network dislocations, and γ is Euler's constant, ~ 0.5772. Parameter L_α is a

length that governs the range of interactions between dislocations and defects, and is defined in Eq. 5.20.

$$L_\alpha = (1+\nu)\mu b|\triangle V_\alpha|/3\pi(1-\nu)kT \tag{5.20}$$

ΔV_α is the relaxation volume of the defect, and its typical value is -0.5Ω for vacancy and 1.2Ω for interstitial. The difference of L_α between vacancies and interstitial has been considered as the cause for irradiation induced swelling. If the sink for vacancies is only from dislocation network, the sink strength for mobile dislocation is defined as Eq. 5.21

$$k_{\alpha N}^2 = -2\pi\rho_N / ln(\rho_N^{1/2} L_\alpha) \tag{5.21}$$

The transfer of defects into jogs on the dislocation is governed by Eq. 5.22

$$\eta_\alpha = c_j b(a_{\alpha c} v_{\alpha c}) exp(-\triangle W_\alpha / kT) \tag{5.22}$$

where c_j is the jog concentration, $a_{\alpha c}$ and a_α are the geometric factors of jumps in core and lattice, $v_{\alpha c}$ and v_c are the attempt frequency for jumps in core and lattice, and ΔW_α is the difference in activation energy for absorption to dislocation and lattice migration. In this model, formulation have proposed by Argon and Moffatt[4] is used to define transfer parameter as in Eq. 5.23

$$\eta_\alpha = 10^3 f_\alpha c_j b(\Gamma/\mu b)^2 \tag{5.23}$$

where Γ is the stacking fault energy.

Taking transfer rate into account, Eq. 5.19 becomes Eq. 5.24

$$k_{\alpha d}^2 = 2\pi\eta_\alpha\rho_N/[1-\eta_\alpha ln(\rho_N^{1/2}L_\alpha)] \tag{5.24}$$

Adopting treatment Hirth and Lothe [33] on the sink strength for dipoles, the effective sink strength for each dislocation in the dipole is defined as Eq. 5.25:

$$k_{\alpha d}^2 = 2\pi\eta_\alpha\rho_N/[1-\eta_\alpha ln(k_\alpha^2 L_\alpha s)] \tag{5.25}$$

where s is the dipole separation distance.

Assuming no damage caused by radiation, flow rate of vacancy to dislocation is defined as Eq. 5.26

$$\frac{dq_d}{dt} = k_{vd}^2 D_s\sigma_c\Omega/kT \tag{5.26}$$

where the lattice self-diffusion coefficient $D_s = D_v c_v^e$.

The climb velocity is defined as Eq. 5.27

$$v_c = (dq_d/dt)/b\rho_d \tag{5.27}$$

Based on Eqs. 5.14, 5.25, 5.26, and 5.27, the separation rate of dipole can be defined is Eq. 5.28

$$ds/dt = -2\eta D_s\mu\Omega/(1-\nu)skT[1-\eta ln(k_\alpha^2 L_\alpha s)] \tag{5.28}$$

Eq. 5.28 can be solved by integrated from the initial dipole separation s_0 as defined in Eq. 5.29

$$\tau = -\frac{(1-\nu)kT}{4D_s\mu\Omega}s_0^2[\eta_v ln(k_v^2 L_v s) - \frac{\eta_v}{2} - 1] \simeq \frac{s_0}{4v_c} \tag{5.29}$$

The thermal recovery rate of mobile dislocation is defined as in Eq. 5.30, by assuming all dislocations are involved in the recovery process, and the initial dipole separation is $s_0 = \rho_m^{-1/2}$.

$$\dot{\rho_m} = -\frac{2\rho_m}{\tau} = -8\rho_m^{3/2} v_{cm} \tag{5.30}$$

The thermal recovery rate of static dislocation is defined as Eq. 5.31 , by assuming that the initial dipole separation is $s_0 = h$ and $k_v^2 = 1/h^2$.

$$\dot{\rho_s} = -\frac{2\rho_s}{\tau} = -8\rho_s \frac{v_{cs}}{h} \tag{5.31}$$

A possibility of diffusion through the lattice replaced by dislocation core diffusion is also considered in this model. The flux of vacancies along the dislocation is defined in Eq. 5.32.

$$j_p = 2\eta_v D_p \sigma_e \Omega / (b + \eta_v L_p) kT \tag{5.32}$$

where η_v is the transfer coefficient of vacancies from dislocation to jogs. D_p is the coefficient for core diffusion, and L_p is the length for the diffusion along the core. If jog spacing is much less than the path length for diffusion, Eq. 5.32 is simplified to Eq.5.33

$$j_p = 2D_p \sigma e \Omega / L_p kT \tag{5.33}$$

The climb velocity is finally defined as Eq.5.34.

$$v_c = 2\pi b D_p \sigma_c \Omega / L_p^2 kT \tag{5.34}$$

5.1.6 Dynamic Recovery

The dynamic recovery is also considered in this model. Without dynamic recovery, material will go stronger and stronger caused by strain hardening without the bound. Dynamic recovery explains the saturation of strain hardening [75] caused by annihilation of mobile dislocations with opposite signs. When this annihilation reach certain rate, the total density of mobile dislocation will stay almost constant. This mechanism was first recognized by Johnson and Gilman[37], and Webster[78]. It is defined as Eq. 5.35 to explain the saturation of strain hardening.

$$\dot{\rho_m} = -\delta(\dot{\rho_m} + \rho_s)\dot{\varepsilon}/b = -\delta\rho_m(\rho_m + \rho_s)v_g \tag{5.35}$$

where δ is the critical distance between dislocations. Annihilation of dislocation with opposite sign will occurs spontaneously when their distance is less than this value [12][22].

5.1.7 Stability of Subgrains

Three processes control the size and nucleation of subgrain [25]. The subgrain size can coarsen due to reduction of the effective subgrain boundary energy; new subgrains can nucleate within the subgrains due to population of dislocations; new subgrains can nucleate within the existing dislocations. As the generation and growth of the general second new phase, growth of subgrains can be treated as the product of a driving force and mobility.

The grain boundary energy per unit area, γ_{sb} for low-angle subgrain boundary can be defined as Eq. 5.36:

$$\gamma_{sb} = -\frac{\mu b^2}{4\pi(1-\nu)}\rho_b R_{sb} ln(bR_{sb}\rho_b) \simeq \frac{\mu b^2}{3}\rho_b R_{sb} \tag{5.36}$$

The total energy of one subgrain E, is defined as $4\pi R_{sb}^2 \gamma sb$. The total driving force acting on a boundary for a collapsing subgrain can be defined as 5.37

$$\frac{dE}{dR_{sb}} = \frac{\partial E}{\partial R_{sb}} + \frac{\partial E}{\partial \rho_b}\frac{d\rho_b}{dR_{sb}} \tag{5.37}$$

The pressure as a driving force for subgrain to grow is defined as Eq. 5.38.

$$P_{sb} = (1/4\pi R_{sb}^2)(dE/dR_{sb}) = (4/3)\mu b^2 \rho_b \tag{5.38}$$

The movement is assumed to be the combination of dislocations glide and climb within the subgrains. The core mobility can be roughly defined as Eq 5.39.

$$M_{sb}^c = 2\pi b D_p \Omega / h^2 kT \tag{5.39}$$

For lattice diffusion, the mobility is defined as Eq. 5.40:

$$M_{sb}^L = 2\pi \eta_v D_v \Omega / h^2 kT \tag{5.40}$$

If precipitates are considered in the model, for dislocation to move through precipitates, the pressure of growth must satisfy Eq. 5.41[9, 59].

$$P_{sb} \geq 2\pi r_p^2 N_p \gamma_{sb} \tag{5.41}$$

If 5.41 is satisfied, then the subgrain growth rate can be approximately defined as Eq. 5.42

$$\partial R_{sb}/\partial t = M_{sb}(P_{sb} - 2\pi r_p^2 N_p \gamma_{sb}) \tag{5.42}$$

Mobility of precipitate motion by self-diffusion in the matrix is defined as Eq. 5.43

$$M_{sb} = D_s \Omega / 4\pi r_p^4 N_p kT \tag{5.43}$$

The driving force for nucleation can be assumed as the form $\mu b(\rho^{1/2} - K_c/2R_{sb})$, where ρ is the total density of the mobile and static dislocations. K_c is a constant with a value around 10 [27, 28] derived from Holt analysis. The time to nucleate the new subgrain configuration can be defined as Eq. 5.44

$$\tau = (kT/\mu\eta_v K_c \rho^{1/2} D_s)[\rho^{1/2} - (Kc/2Rsb)]\Omega \tag{5.44}$$

To reach a new configuration, dislocations have to move a distance of about $K_c\rho^{1/2}$. The change of cell radius is $R - (K_c/2\rho^{1/2})$. The rate equation 5.45 for subgrain can be obtained by combining all these expression .

$$\partial R_{sb}/\partial t = -\mu\eta_v K_c R_{sb}[(\rho_m + \rho_s)^{1/2} - (K_c/2R_{sb})]^2 \Omega D_s/kT \tag{5.45}$$

Eq. 5.45 can be used only when $(\rho_m + \rho_s)^{1/2} > K_c/2R_{sb}$ is satisfied.

5.1.8 Constitutive Behavior

As general plasticity method, total applied strain can be split into elastic and plastic portion as defined in Eq. 5.46

$$\varepsilon^{tot} = \varepsilon^e + \varepsilon^p \tag{5.46}$$

According to Hooke's Law, stress and strain relation can be defined as Eq. 5.47

$$\sigma = E\varepsilon^e \tag{5.47}$$

where E is the young's modulus. Plug Eq. 5.46 into Eq. 5.47, and take derivative to time to define Eq. 5.48. This equation is later used as one of six ODEs, Eq. 5.54, to extract the strain stress relation of material.

$$\dot{\sigma} = E(\dot{\varepsilon}^{tot} - \dot{\varepsilon^p}) \tag{5.48}$$

5.1.9 Summary of Model Equations and Solution Approach

Six ordinary differential equations are setup as following.

Orowan Equation:

$$d\varepsilon^p/dt = b\rho_m v_g \tag{5.49}$$

Mobile Dislocation Density:

$$\frac{\partial \rho_m}{\partial t} = v_g[\rho_m^{3/2} + \frac{\beta R_{sb}}{h^2} - \frac{\rho_m}{2R_{sb}} - 8\rho_m^{3/2}(\frac{v_{cm}}{v_g}) - \delta\rho_m(\rho_m + \rho_s)] \tag{5.50}$$

Static Dislocation Density:

$$\frac{\partial \rho_s}{\partial t} = v_g[(\frac{\rho_m}{2R_{sb}}) - 8\frac{\rho_s}{h}(\frac{v_{cs}}{v_g}) - \delta\rho_m\rho_s] \tag{5.51}$$

Boundary Dislocation Density:

$$\frac{d\rho_b}{dt} = 8(1-2\zeta)\rho_s\frac{v_c}{h} - (\frac{\rho_b}{R_{sb}})M_{sb}(p_s - 2\pi r_p^2 N_p\gamma_{sb}) \tag{5.52}$$

Subgrain Radius:

$$\frac{dR_{sb}}{dt} = M_{sb}(p_s - 2\pi r_p^2 N_p\gamma_{sb}) - \mu\eta_v K_c R_{sb}[(\rho_m + \rho s)^{1/2} - \frac{K_c}{2R_{sb}}]\frac{\Omega D_s}{kT} \tag{5.53}$$

Table 5.1: Model output

Parameter	Unit
Plastic Strain, ε^p	cm/cm
Mobile Dislocation Density, ρ_m	$1/cm^2$
Static Dislocation Density, ρ_s	$1/cm^2$
Boundary Dislocation Density, ρ_b	$1/cm^2$
Subgrain Radius, R_{sb}	cm

A strain stress relation was added to derive the self-hardening effect caused within this slip system. We use here a constant strain rate condition.

$$\frac{d\sigma}{dt} = E(\frac{d\varepsilon^{tot}}{dt} - b\rho_m v_g) \tag{5.54}$$

These ODEs are solved with the forward Euler method with a very small step. The maximum applied step in this model was decided by running many cases with different size of step until it converges. The whole model is coded as a subroutine embedded in ABAQUS user's subroutine Umat.

5.2 Parameter Calibration for Self-Hardening in Copper

To fit this model to define self-hardening effects in copper with crystal plasticity model, some material's parameters need to be calibrated.

Microstructure Evolution was computed at each integration point and recorded. The units of microstructure are listed in table 5.1.

5.2.1 Calibration of Model Parameters

Self-hardening behavior of each slip system has been calibrated to fit the mechanical properties of copper. Table 5.2 shows the influence of parameters in the dislocation-based model on the mechanical behavior, while and 5.3 shows the calibrated parameters for copper at 25 C.

Table 5.2: The calibrated parameters and the influence on mechanical behavior of materials

Parameter	Unit	Affected Property
Initial Mobile Dislocation Density, $\rho_m(0)$	$1/cm^2$	Yield Strength
Initial Static Dislocation Density, $\rho_s(0)$	$1/cm^2$	Yield Strength
Initial Boundary Dislocation Density, $\rho_b(0)$	$1/cm^2$	Yield Strength
Jog Concentration, X_{jog}	-	Yield Strength
Activation Volume, Q	Ω	Yield Strength
Critical Dislocation Spacing, δ	cm	Elasto-plastic tangent
Precipitate Radius, r_p	Å	Yield Strength
Precipitate Concentration, N_p	cm^3	Yield Strength
Dislocation Vibration Frequency, ν_d	sec^{-1}	Yield Strength

Table 5.3: Values of calibrated parameters

Parameter	Units	Copper
Initial Mobile Dislocation Density, $\rho_m(0)$	$1/cm^2$	1E10
Initial Static Dislocation Density, $\rho_s(0)$	$1/cm^2$	1E9
Initial Boundary Dislocation Density, $\rho_b(0)$	$1/cm^2$	1E9
Critical Dislocation Spacing, δ	cm	4E-6
Precipitate radius, r_p	$\mathring{A}$	40.5 (at 25 C)
Dislocation Vibration Frequency, ν_d	sec^{-1}	1E12

Table 5.4: Constants of copper in the model

Parameter	Units	Value of Copper
Glide energy, E_{glide}	eV	1.87
Self energy, E_{self}	eV	2.4
Diffusion coefficient, D_0	cm^2/s	0.2
Burger's vector, b	cm	2.58E-8
Atomic volume, Ω	cm^3	1.19E-23
Precipitate concentration, N_p	cm^3	1.63E19 (at 25 C)
Jog fraction, X_{jog}	-	0.0455
Activation volume, Q	Ω	21.5 (at 25 C)

CHAPTER 6

Results and Comparison with Experiments

We present here the results of computer simulations for plastic deformation of pure copper. We first use the isotropic plasticity framework to study the distribution of plastic strain in a standard polycrystalline copper tensile sample. This will serve as reference for subsequent simulations of single and polycrystalline copper, and to show the fundamental differences in the spatial distribution of plastic strain when we compare isotropic plasticity to crystal plasticity results. The mechanical deformation of copper polycrystals is finally presented to examine grain size effects on the deformation characteristics..

6.1 Isotropic Plasticity

This model is built by coupling isotropic plasticity theory discussed in chapter 3 and dislocation density based model discussed in chapter 5. The hardening law in isotropic plasticity is defined by the dislocation density based model.

Pure copper was used in this simulation. Young's modulus is : 130 Gpa, poisson's ratio is : 0.32 [13]. A dog-bone like sample was constructed with the pinned boundary conditions at the left-hand end and applied displacement at the right-hand end. The applied strain was increased up to 15%.

The results of our computer simulations are shown in Figure 6.1, where the distributions of the equivalent von Mises stress, plastic strain, mobile dislocation

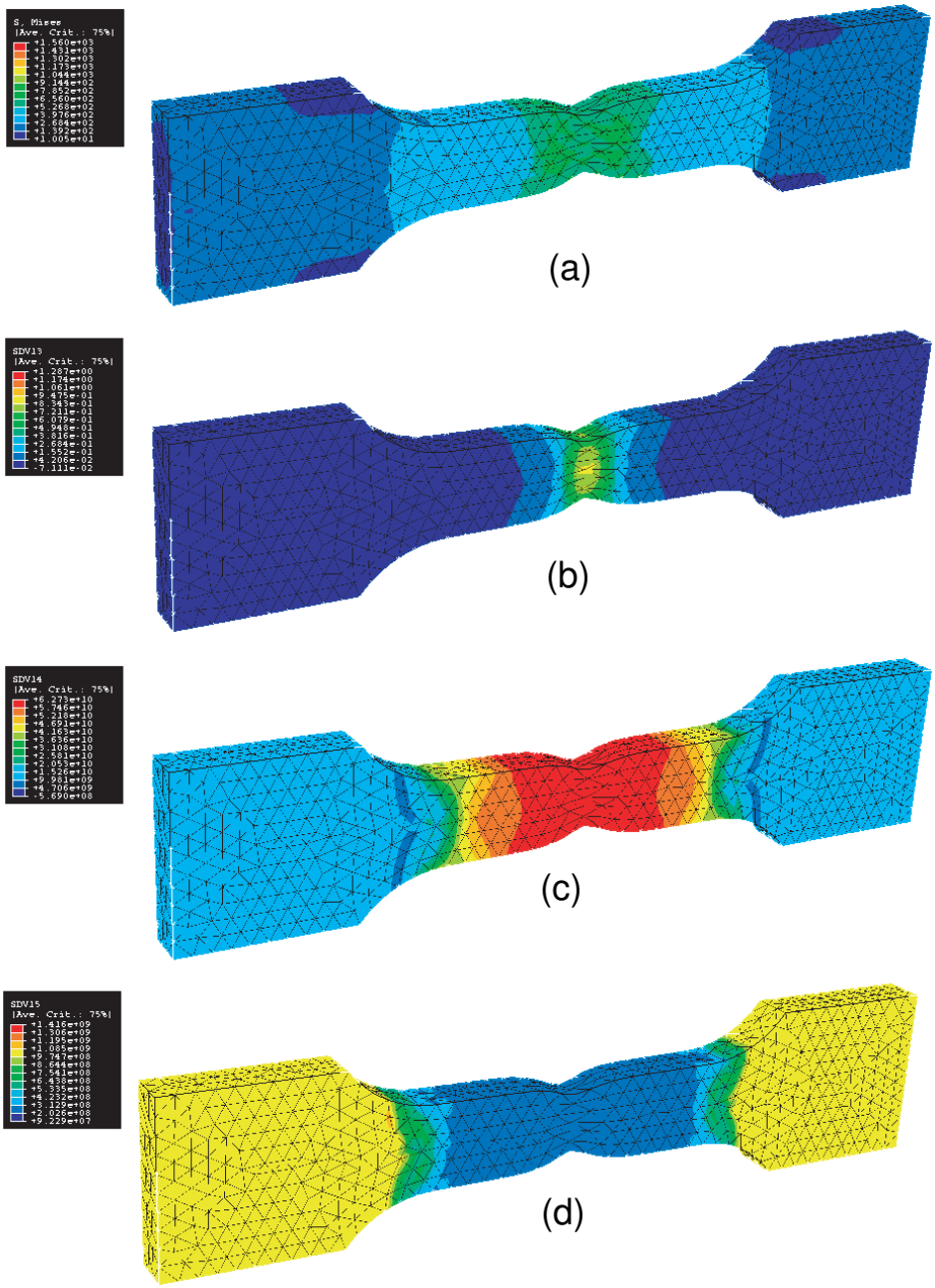

Figure 6.1: Simulation results based isotropic elasticity and plasticity coupled with dislocation density based model. (a) von Mises stress. (b). Plastic strain. (c) Distribution of mobile dislocation. (d). Distribution of static dislocation.

density and static dislocation density are shown. It is clear that the model reproduces the well-known necking instability observed in ductile metals. Nevertheless, the isotropic plasticity model does not allow us to study the internal heterogeneous distribution of plastic strain, as we will see in the following simulations with our crystal plasticity model.

These results show the great necessity to develop a method with an inherent capability to resolve on different crystallographic orientations, and to associate such anisotropic distribution with the underlying microstructure.

6.2 Simulation Results of $3D$ Crystal Plasticity Model

6.2.1 Simulation Results of a Single Crystal

A $3D$ single crystal model is constructed as shown in figure 6.2. The dimensions of the sample are $100\mu m \times 11\mu m \times 2.5\mu m$. An initial imperfection at the center of the sample as a through-thickness square hole with $size = 1\mu m$ is used to initiate shear bands by concentrating the stress in its vicinity. The shear band patterns depend on the configuration of the initial imperfection [52]. The initial crystallographic orientation of the two slip planes is at $\theta = 45°$. Quadratic brick elements with reduced integration are employed in this simulation.

Two displacement boundary conditions are applied to two ends.

- At the left end, we use: $u_1 = 0, \quad u_2 = 0, \quad u_3 = 0$
- At the right end, we use: $u_1 = 8\mu m, \quad u_2 = 0, \quad u_3 = 0$

As shown in figure 6.3, two stripes consisting of large deformed elements cross and form double shear bands as observed in experiments [52]. Elements around

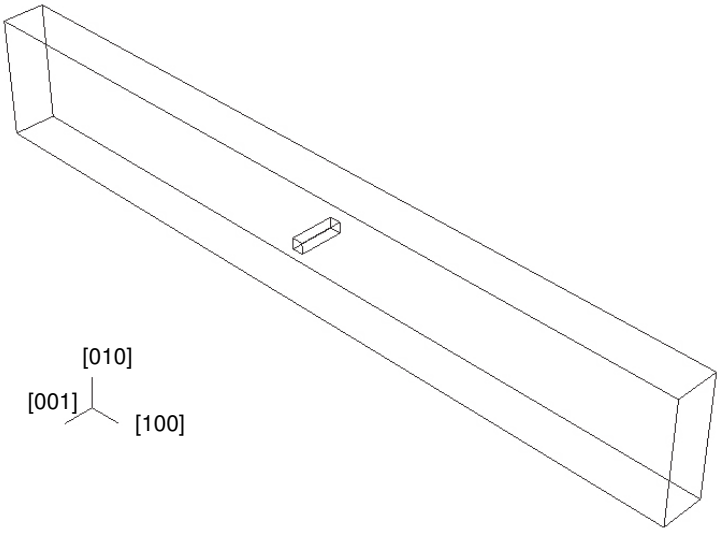

Figure 6.2: $3D$ single crystal plasticity model with an initial imperfection at the center of the sample

shear bands were not deformed, which means that once the shear bands are initiated, they are highly confined to the favorable orientation and show highly heterogeneous deformation behavior. Another observation, which can be seen clearly is the formation of necking in the middle of the sample.

The distribution of plastic strain ε_{11} and ε_{22} are shown in figure 6.4. According to the applied displacement boundary conditions, the total strain is 8%. Since the elastic strain is very small, the applied strain is almost all plastic. However, the area outside the shear bands has plastic strain of less than 4%, indicating that the majority of the plastic strain concentrates within two shear bands. The lowest plastic strain ε_{11} is around 15%, and the highest plastic strain appearing around the upper side of the imperfection reaches 75%. This heterogeneous plastic deformation agrees with experimental observation by Elam [21]. Many simulations with different initial imperfection configurations were also per-

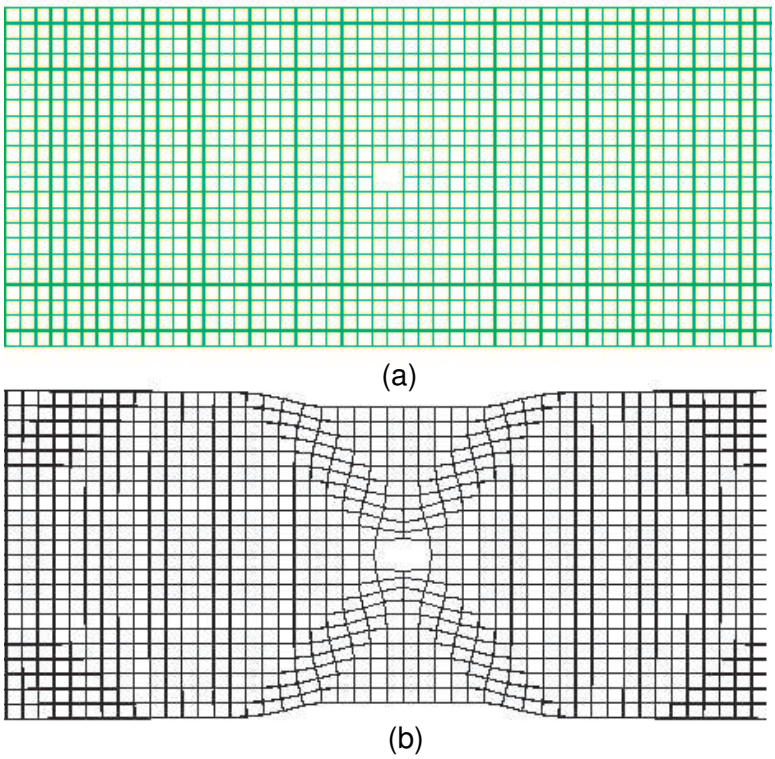

Figure 6.3: (a). Initial shape. (b). Deformed shape.

formed, such as with different positions of the initial imperfection in the sample. It is shown that the shear band pattern depends on the configurations of initial defects. The magnitude of plastic strain ε_{22} shows the same distribution since the sum of these two plastic strains is zero as a result of volume conservation of plastic deformation.

Figure 6.5 (a) shows the initial crystallographic orientation is 45° according to the defined convention. (b) clearly shows that the net crystallographic misorientation within the shear bands is as high as 19.36° and that the lattice rotations within two shear band have opposite directions. However, the lattice within the two shear bands rotate to facilitate plastic slip and hence increase the Schmid

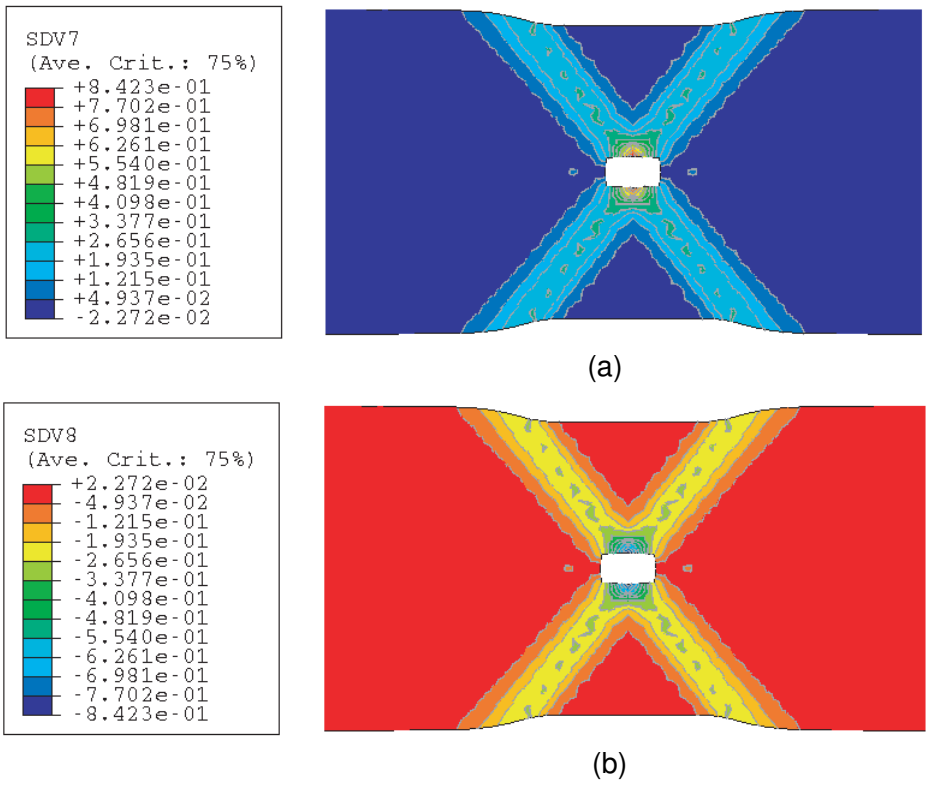

Figure 6.4: (a). Spatial distribution of plastic strain ε_{11}. (b). Spatial distribution of plastic strain ε_{22}

tensor. This explains the so called geometric softening. Rotation of the lattice results in a higher Schmid stress, which, in turn, produces larger plastic slip. Thus, and instability is initiated. Figure 6.5 (c) shows that final crystallographic orientation within one shear band reaches 64.36°, and the counterpart in the conjugate shear band drops to 25.64°.

The density distribution of the mobile and forest (static) dislocations in the single crystal are shown in Figures 6.6 (a) and (b), respectively. Only the left half of the sample is shown because of symmetry. It is interesting to note that while

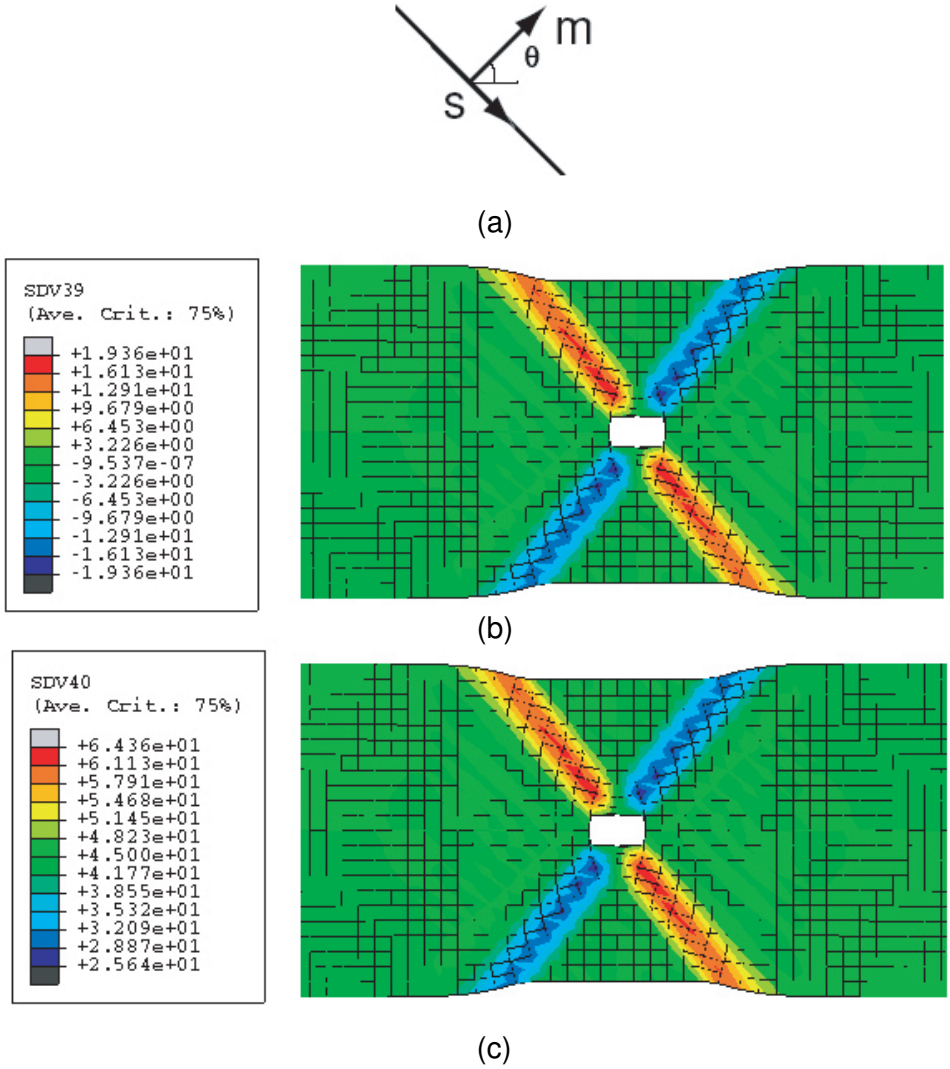

Figure 6.5: (a). Initial crystallographic orientation is 45 degree. (b). Lattice rotation. (c). Final crystallographic orientation

the mobile dislocation density is the highest near the shear bands, this is not the case for the forest dislocations, which tend to be depleted as a result of the high generation rate of the mobile dislocation density. The dislocation densities are shown in units of cm^{-2}.

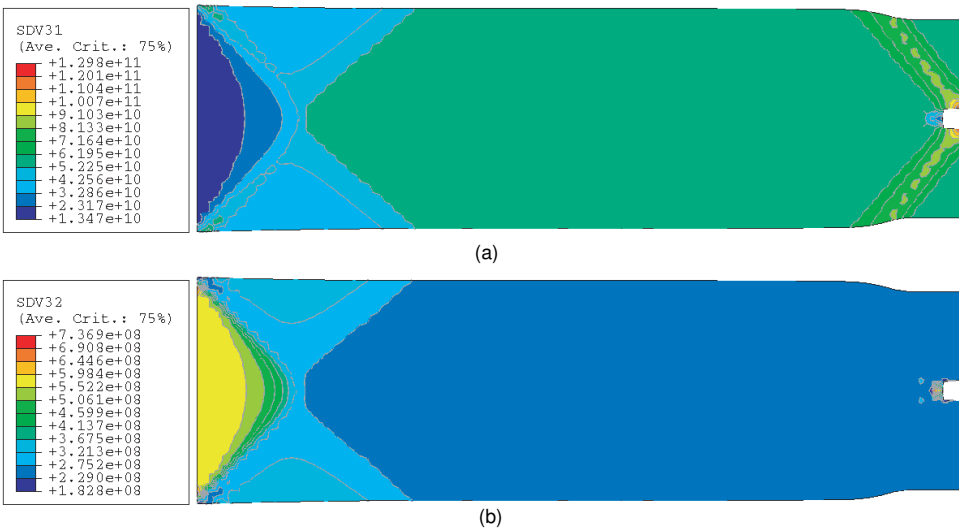

Figure 6.6: Density distribution of mobile dislocations (a), and forest (static) dislocations (b). Densities are shown in cm^{-2}.

Figure 6.7 shows the strain stress curves of single crystal copper with different initial crystallographic orientations. Initially, the crystal is rotated to a specified orientation, while the global applied stress is uniaxial (i.e. along the 1-direction). The changes in the yield behavior is a result of variations of the Schmid stress, as the global stress is projected on the slip plane. Further variations in the hardening behavior is a result of the large deformation associated with crystal rotation as it continues deforming. The highest stress achieved is obviously at $\theta = 45°$ because this would correspond to the highest Schmid stress. The plastic instability commences at a strain of about 4.2%, which corresponds to the beginning

of necking and large lattice rotation.

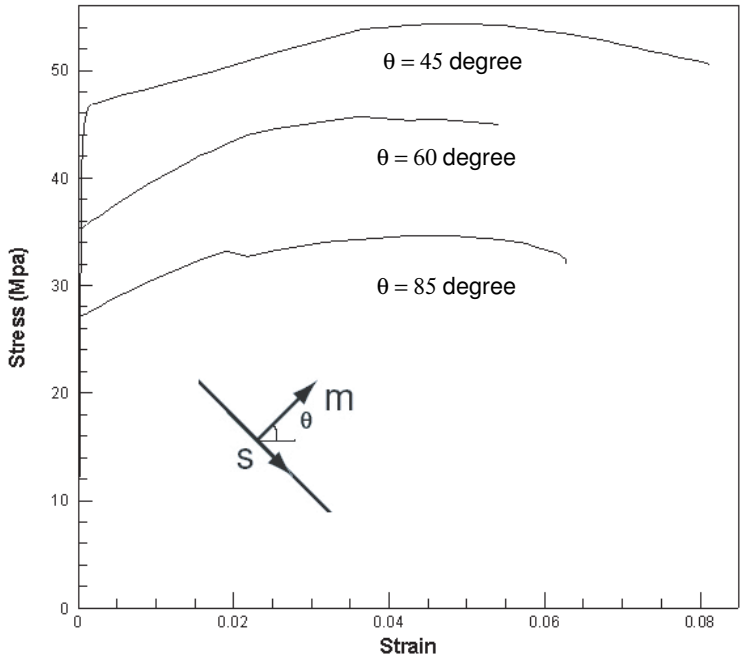

Figure 6.7: Stress-strain behavior of single crystal copper with different initial crystallographic orientations of single crystal

6.2.2 Plastic Deformation of a Bi-crystal

Simulation conditions:

- Initial geometry is a parallelepiped : $80\mu m \times 35\mu m \times 1.0\mu m$
- Initial crystallographic orientations:
  - Left crystal: $\theta =$ 60°
  - Right crystal: $\theta =$ 25°
- Boundary conditions:

- Left side: $u_1 = 0, \quad u_2 = 0, \quad u_3 = 0$
- Right side: $u_1 = 6.4 \quad \mu m, \quad u_2 = 0, \quad u_3 = 0$

- The grain boundary between the two crystals is assumed to be perfect, with no possibility of glide or separation.

Figure 6.8 shows the distribution of lattice orientations for the bicrystal, with (a) initial orientations; (b) final orientations, and (c) lattice misorientations. It is shown that because of the initial favorable orientation of the right side crystal, the Schmid stress is the highest on the slip planes, and a shear band is initiated at the triple point junction between the two crystals and the free surface. The right side crystal rotates significantly during deformation, inducing localized rotation of the left-side crystal in the zone with the highest stress. Since grain boundary sliding is prevented in the present simulation, the confinement effect of the let crystal leads to geometric hardening, while the continued rotation of the right-side crystal results in geometric softening and instability.

Figure 6.9 shows the spatial distribution of the plastic strain component ε_{11}. It is seen that local values of up to 38% are achieved in the bicrystal, with an average strain of 27% within the shear band. In comparing the results of the bi-crystal to the single crystal, we see that both geometric softening and compatibility hardening are at play here, as opposed to geometric softening alone in the single crystal. While crystal lattice rotation and finite strain effects result in the initiation and continuation of the plastic instability of the shear band for the left-side crystal, the requirement of bi-crystal compatibility at the grain boundary hardens the bi-crystal. Another important observation here is that the initiation point of the shear band is clearly at the triple point junction (stress concentration), and an initial defect is not required for initiation.

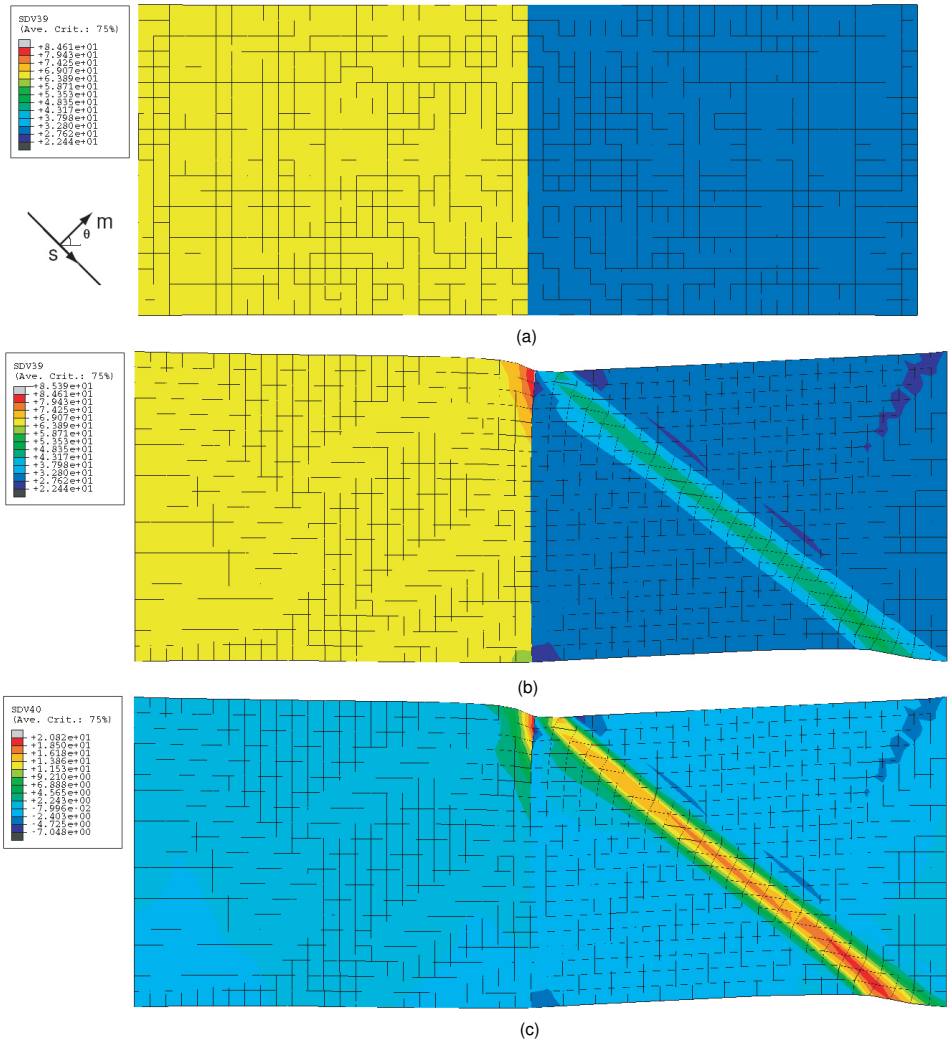

Figure 6.8: Orientations of a copper bicrystal deformed at a total applied strain of 8%. (a) Initial orientations; (b) final orientations, and (c) lattice misorientations.

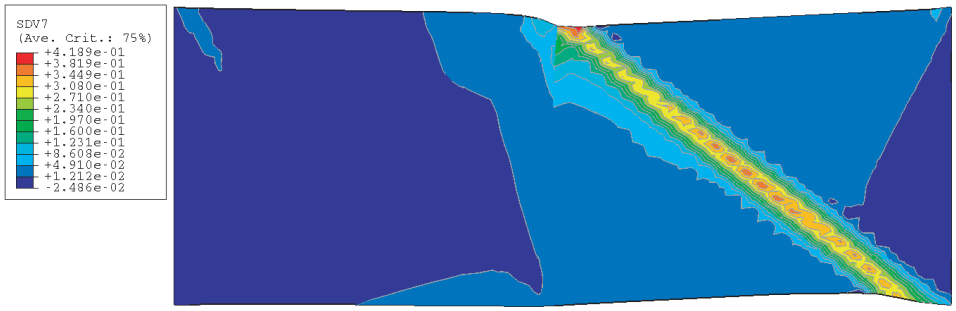

Figure 6.9: Spatial distribution of the plastic strain component ε_{11}.

In the crystal plasticity model, slip is associated with Schmid stress and the yield surface is therefore complex in stress space. The simple isotropic distortion energy theory of plasticity predicts that the yield surface is a sphere when represented in the appropriate stress space. Figure 6.10 shows the distribution of the equivalent or Mises stress in the bicrystal. While the von Mises stress is certainly higher in the shear band areas, it is not directly correlated with plastic strain, as can be seen in the figure.

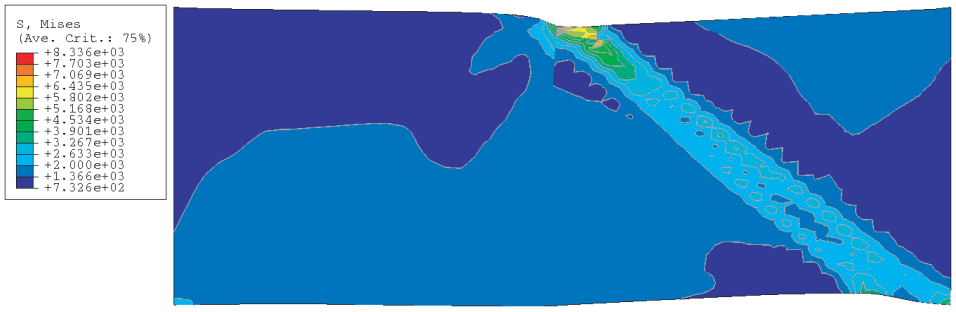

Figure 6.10: Magnitude of von Mises stress within bicrystal. Unit is Mpa

The spatial distribution of the mobile and forest (static) dislocation densities are shown in Figures 6.11 (a) and 6.11 (b), respectively. It is shown here that the mobile density is very well correlated with the accumulated plastic strain via

Orowan's equation. On the other hand, the shear band is depleted from forest dislocations as a result of the generation of mobile dislocations from their forest counter parts and the corresponding destruction by recovery processes.

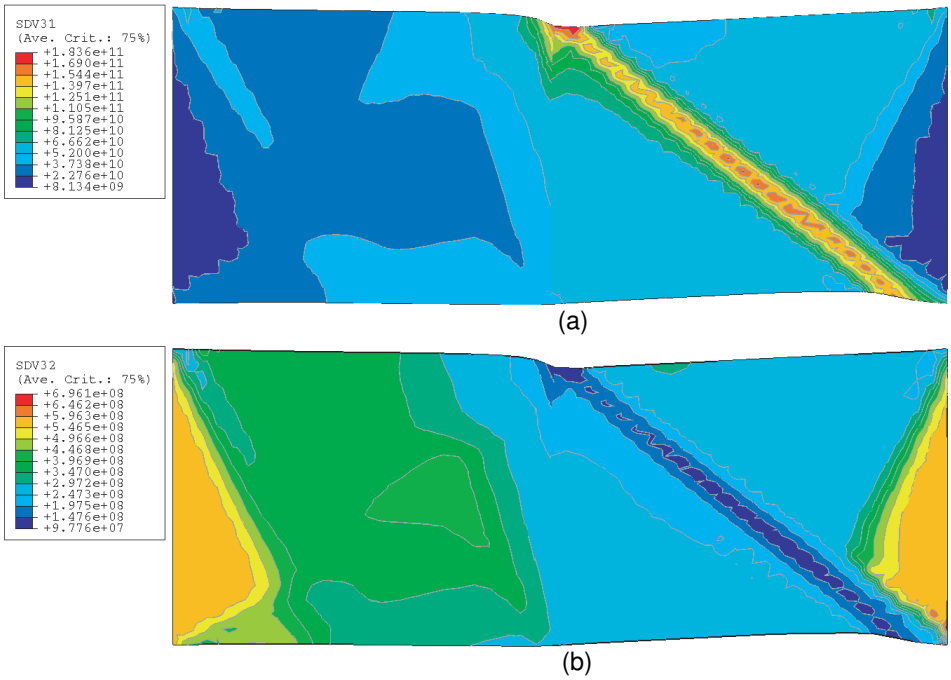

Figure 6.11: Spatial distribution of: (a) the mobile dislocation density; and (b) the forest (static) dislocation density. Densities are in units of cm^{-2}.

6.2.3 Simulation Results of Polycrystal Model Based on Real Crystal Structure

Our simulations begin with a geometric realization of the grain structure of polycrystalline copper. We use the micrographs of copper alloy from works of Cartensen [14], and digitize all grain boundaries. The results of this process are shown in Figure 6.12 (a), which shows the original micrographs of copper alloy [14], and Figure 6.12 (b), which displays the results of our digitization. We then

perform a numerical simulation for the plastic deformation of the polycrystal, with the following boundary conditions: (1). Sample geometry: 35 μm long, 15.5 μm wide, and 1 μm thick; (2). Average grain size = 55 μm; (3). Random initial crystallographic orientations, as indicated by the color map of Figure 6.12 (b); (4). Left boundary conditions: $u_1 = u_2 = u_3 = 0$; and (5). Right boundary conditions: $u_1 = 2.1\mu m, \quad u_2 = u_3 = 0$.

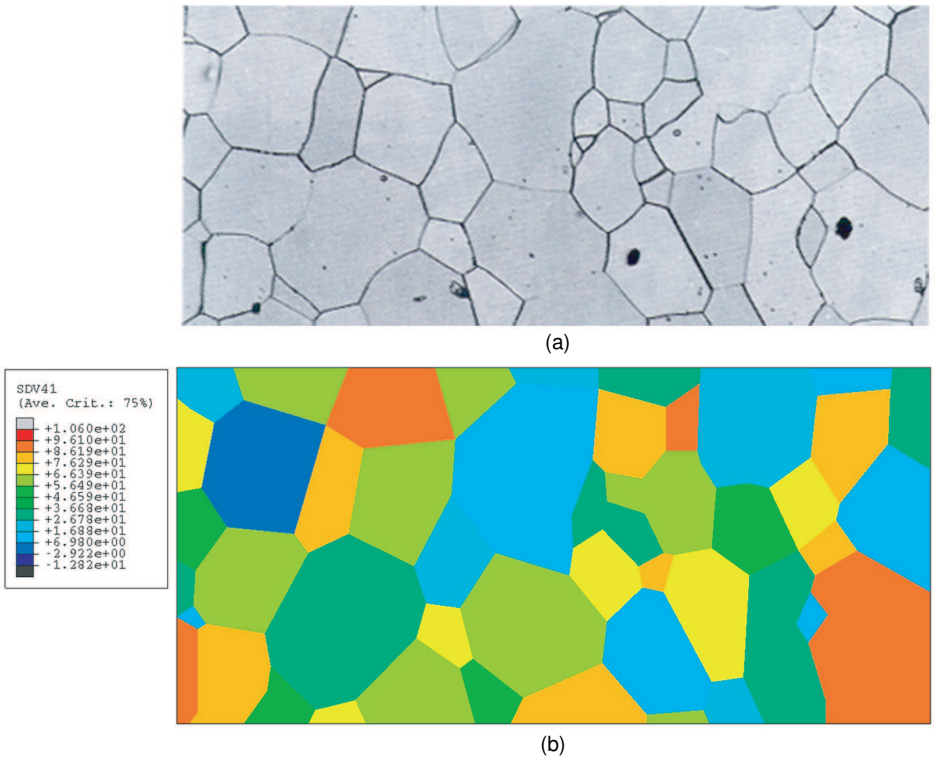

Figure 6.12: (a). Optical microscopic photo of polycrystal copper alloy, adopted from the work of Cartensen [14] (b). Digital rendering of the polycrystalline micrograph shown in (a).

Figure 6.13 (a) shows a contour plot for the rotation of crystallographic orientations in the polycrystalline sample. Figure 6.13 shows the corresponding

contours for the rotation angles, which range from 23° to −25°. Large lattice rotation appear at the surface causing protrusions and intrusions from the original position.

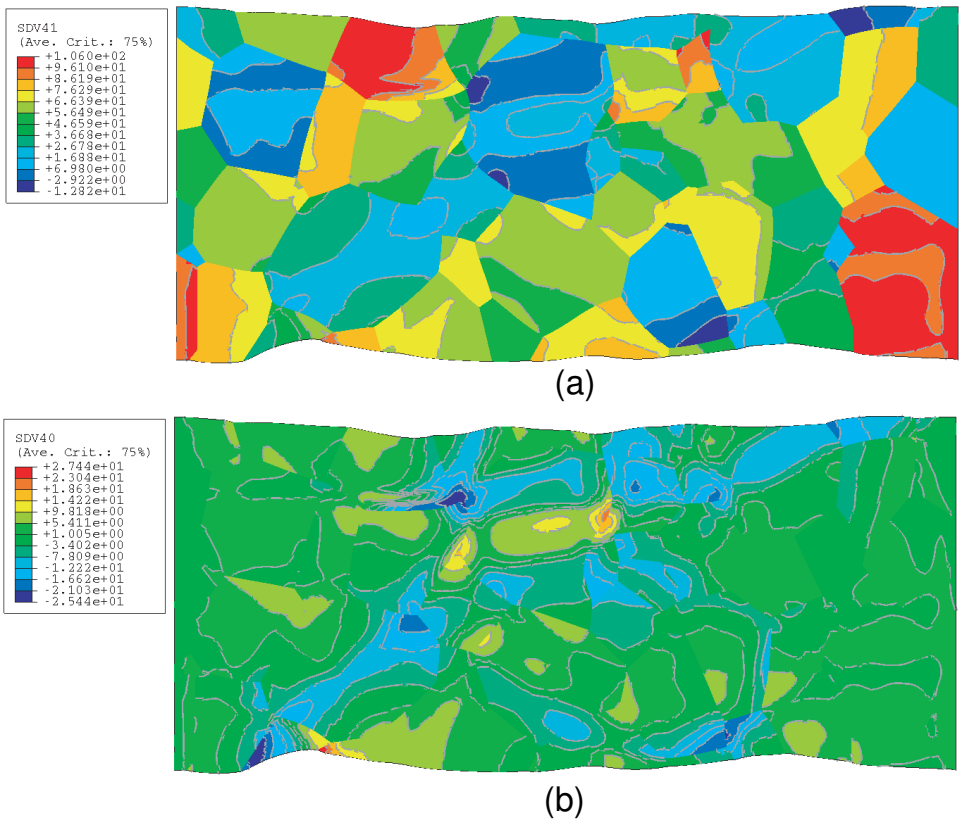

Figure 6.13: (*a*). A contour plot for the final crystallographic orientations in response to an applied strain of 6%. (*b*). A contour plot of net lattice rotations.

Figure 6.14 clearly shows the formation of several shear bands that cut across grains, with plastic strain ϵ_{11} values as high as 45%, and an average value of 20%. Figure 6.14 agree with the experimental results of figure 2.5 which is the formation of shear bands in heavily rolled polycrystalline aluminum observed by Diliamore *et al.* in 1979 [20]. The experimental results show that multi shear bands are formed along preferred orientation, approximately ±45°. simulation

results in figure 6.14 and figure 6.15 show the formation of multi shear bands in the range of $\pm 30^\circ - 45^\circ$

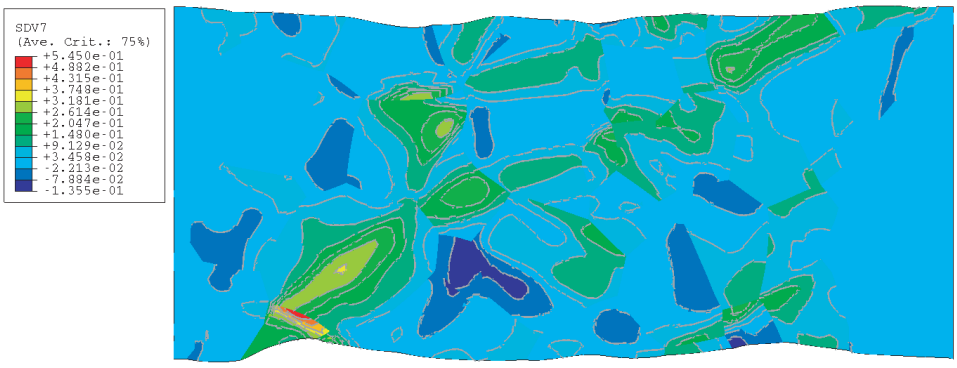

Figure 6.14: (a) A contour plot for the distribution of the plastic strain, ϵ_{11}, in the polycrystalline sample.

To illustrate the statistical nature of shear band formation, we performed additional simulations with the same conditions mentioned above, but for seven different initial random distributions of grain orientations. We show here the results of simulations for three of these cases. Figure 6.15 displays a contour plot of the spatial distribution of the plastic strain component, ϵ_{11}, within each grain of the polycrystalline sample. Each case represents the distribution of plastic strain for a different initial random distribution of grain orientations. Surface roughness and large lattice rotations are in qualitative agreement with experimental observations by Diliamore *et al.* in 1979 [20].

The distribution of the mobile dislocation density is shown in Figure 6.16 as a contour plot. The dislocation distribution is quite heterogeneous, and varies by more than an order of magnitude in neighboring areas, reaching densities as high as $4 \times 10^9 \quad cm^{-2}$

Experimental observations indicate that the grain size has an important effect

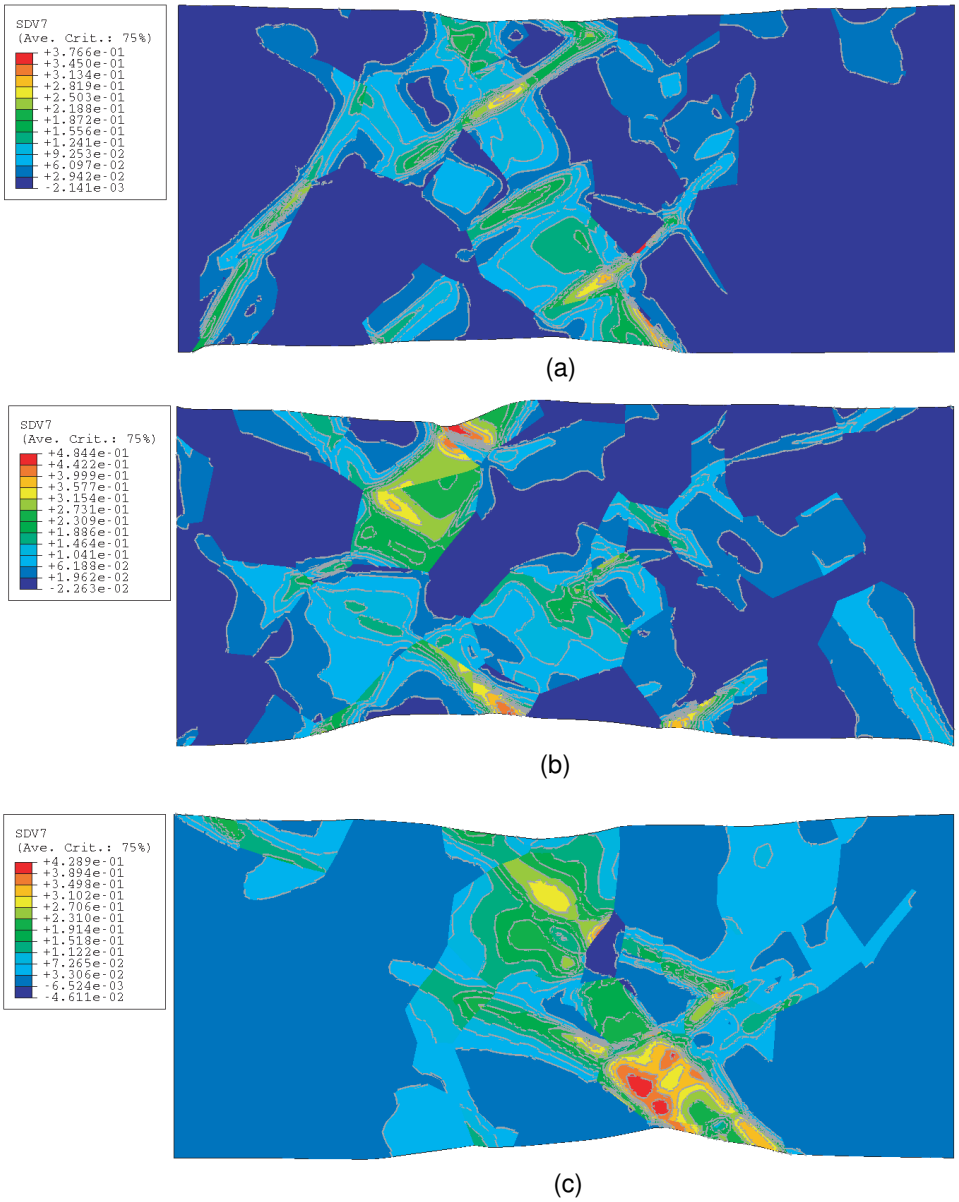

Figure 6.15: Contour plots for the plastic strain ϵ_{11} distribution within each grain. The cases (a), (b), and (c) correspond to different initial random distribution of crystal orientations.

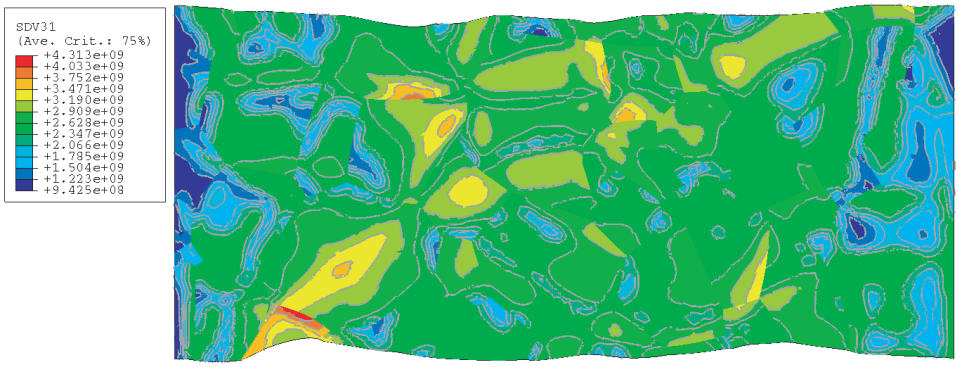

Figure 6.16: Density distribution of mobile dislocations

on the strength metals [13]. The hardening effect of smaller grain size can be attributed to two sources: (1) the Hall-Petch effect, which is a result of confining dislocations in pileup configurations within each grain, and (2) the resistance of grain boundaries to lattice rotations of adjacent grains. In the following, we study the effects of a smaller grain size on the hardening of polycrystalline copper. Although we do not explicitly include the Hall-Petch effect into our model, the results indicate that significant hardening will also result from the confinement of lattice rotations of adjacent grains.

The results of our computer simulations for the stress-strain behavior of polycrystalline copper of different initial orientations and two different average grain size are shown in Figure 6.18. Our results are compared to the experimental data of Singh, (reference [65]), with samples of an average grain size of 55 microns. The initial yield point is clearly elevated by reducing the grain size, and the hardening rate is significantly increased form 1.3 GPa (about $\mu/40$) to 10 GPa (about $\mu/5$). Results of computer simulations for smaller grain size (35 micron) show a significant increase in the yield strength and hardening rates, in qualitative agreement with experiments [14]. The hardening rate for the smaller grain size

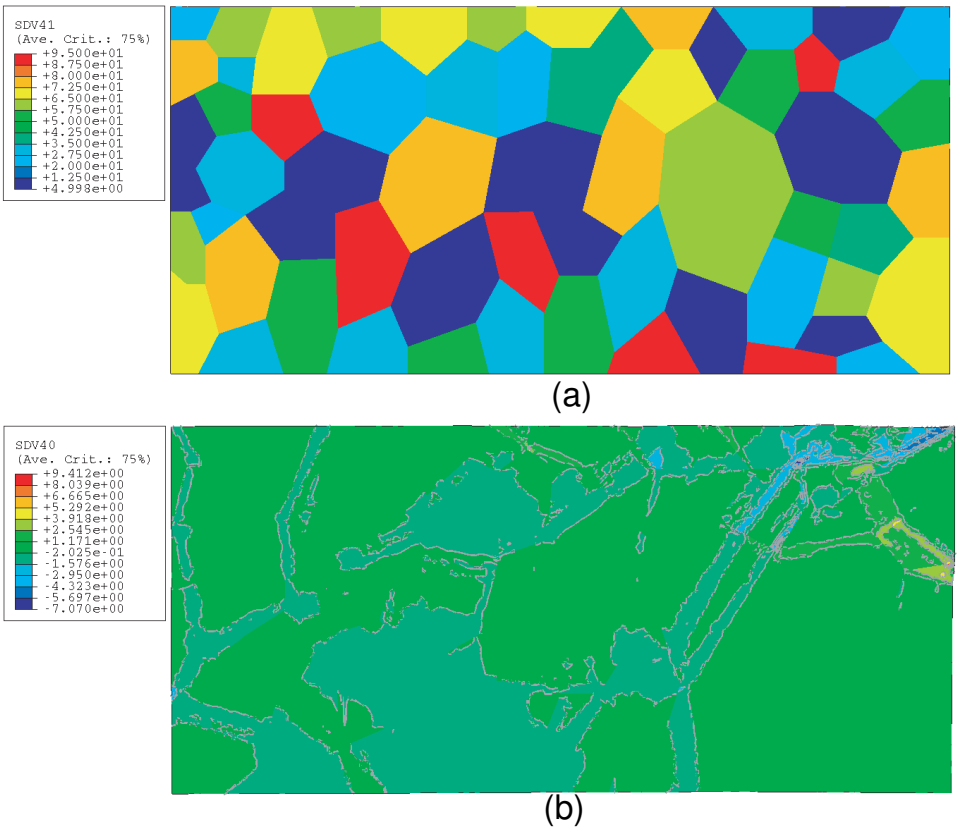

Figure 6.17: (a) Geometric model of polycrsytalline copper alloy, with an average grain size of 35 microns (based on micrographic photo adopted from Carstensen [14]; (b) a contour plot for the distribution of lattice rotations.

specimen is higher than observed experimentally as a result of the lack of grain boundary sliding in our model.

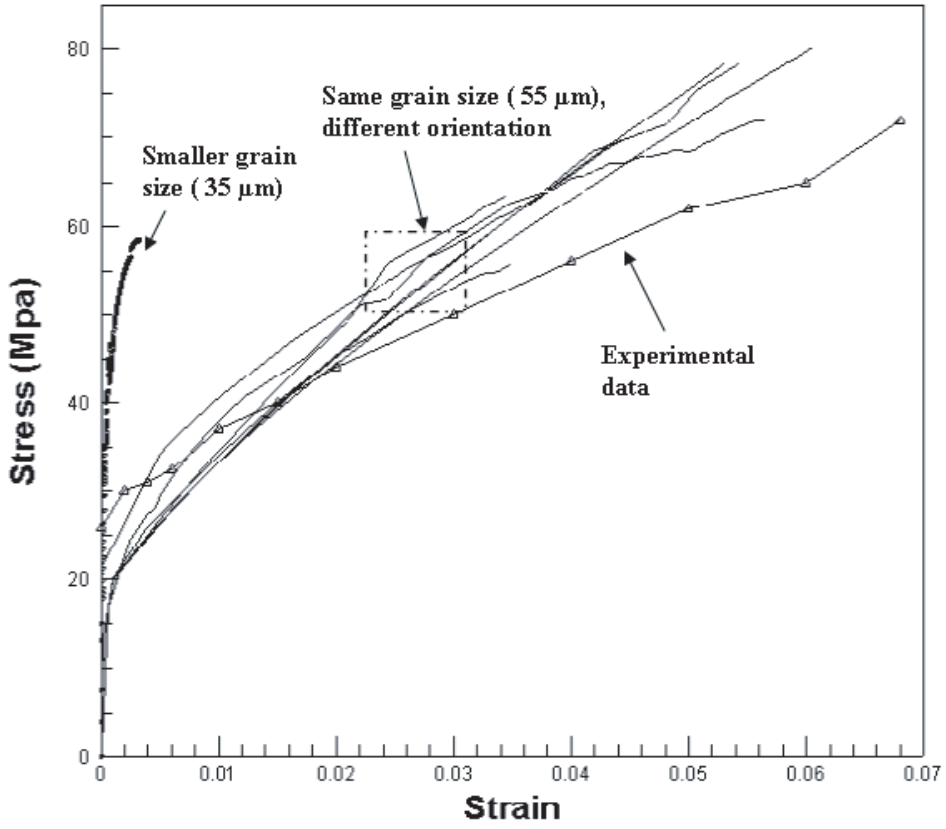

Figure 6.18: Stress-strain curves for polycrystalline copper with an average grain size of 55 microns (solid curves), and 35 microns (dotted curve). Also, we show here the experimental data of Singh. (see reference [65]).

6.3 The Influence of Multiple Slip Systems on Plastic Deformation of Single Crystals

In this section, we present the results of FEM simulations for the plastic deformation of a single fcc crystal. In the present case, we have 24 slip systems (12 in each direction), and the crystal is initially oriented as shown in Figure 6.19, where the sides of the cube are aligned along the crystallographic cube directions.

The single crystal cube is subjected to the following boundary conditions: (the left side has $u_1 = u_2 = u_3 = 0$, while the right end is $u_1 = 5\mu m, \quad u_2 = u_3 = 0$). Quadratic brick elements are used throughout with reduced integration, and the cube side length is taken as 100 μm.

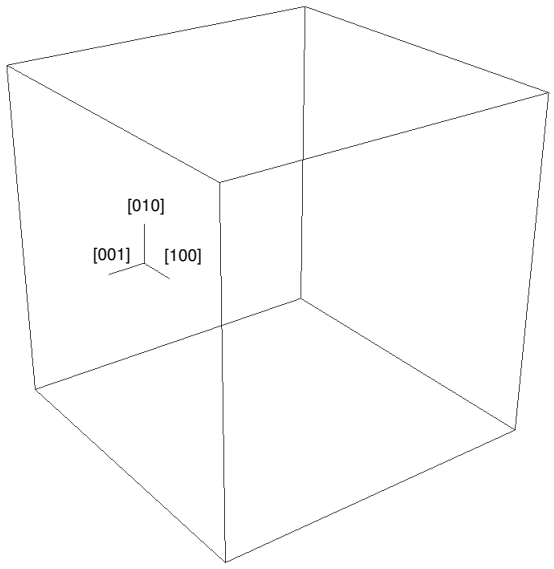

Figure 6.19: A single element model with 12 slip system at initial state

Figure 6.20 illustrates the deformed shape of the single crystal, while the corresponding stress-strain curve is shown in Figure 6.21. The significant increase in the hardening rate in the model with 12 slip systems, as opposed to the model

with 2 slip systems shown in Figure 6.18, is a result of increased latent hardening of the full slip systems of the fcc crystal.

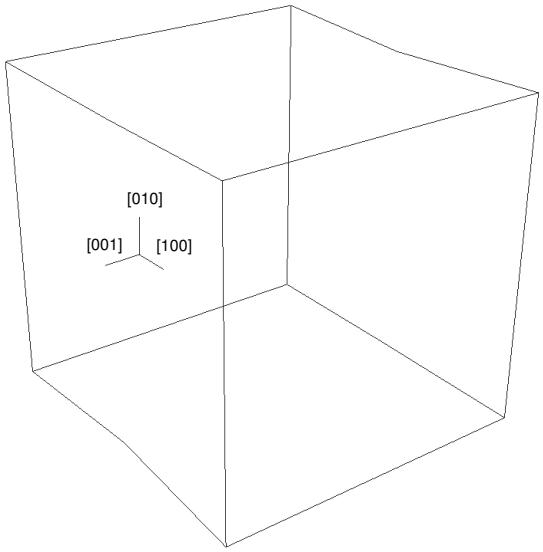

Figure 6.20: Deformed element under tensile stress

According to the initial crystallographic orientation and applied boundary conditions, there exists eight equivalent slip systems in this single crystal, and thus they will accumulate the same amount of plastic strain, as shown in Figure 6.22. When the applied stress reaches around 50 Mpa, plastic yield is initiated and plastic slip occurs on activated slip systems.

Table 6.1 shows the activated slip systems, the corresponding slip direction and plane normal, as well as the Schmid stress on each system for an applied stress of 50 MPa.

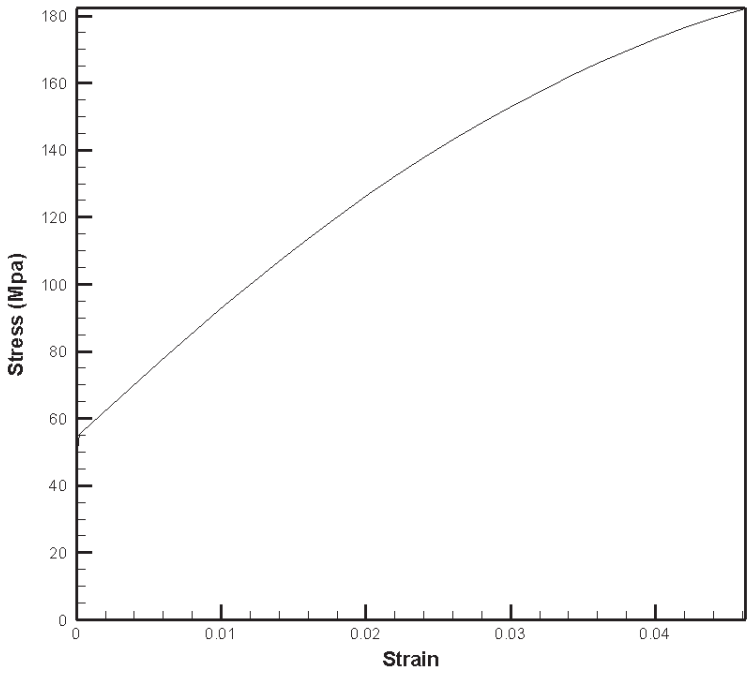

Figure 6.21: The simulated strain stress curve of single copper crystal

Table 6.1: Activated slip systems and the Schmid stress on them

α	s^α	m^α	Schmid stress (Mpa)
3	$[1\bar{1}0]$	(111)	20.41
6	$[\bar{1}\bar{1}0]$	$(\bar{1}11)$	20.41
9	$[\bar{1}\bar{1}0]$	$(\bar{1}1\bar{1})$	20.41
11	$[1\bar{1}0]$	$(11\bar{1})$	20.41
12	$[101]$	$(11\bar{1})$	20.41
14	$[10\bar{1}]$	(111)	20.41
17	$[\bar{1}0\bar{1}]$	$(\bar{1}11)$	20.41
20	$[\bar{1}01]$	$(\bar{1}11)$	20.41

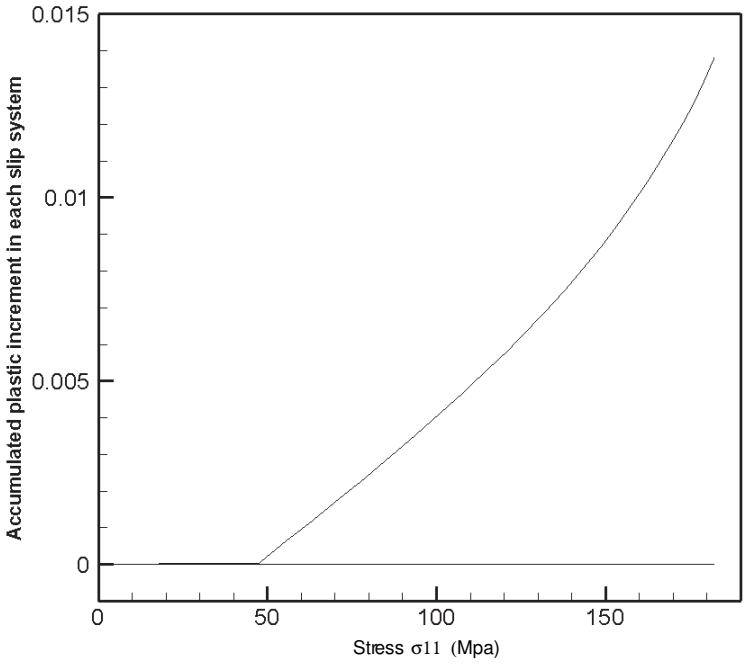

Figure 6.22: Accumulated plastic increment within each slip system

CHAPTER 7

Conclusions and Suggestions for Future Research

The research presented in this thesis has focused on an effort to incorporate a physical model of plastic deformation into the framework of crystal plasticity and to demonstrate the origins of strain localization.The thesis is devoted to the study of mechanical instabilities, which give rise to microstructure pattern formation and eventual failure of stressed solids, because of the strong link between mechanical instabilities and failure.

Strain localization and dislocation microstructure formation are characteristic features of the plastic deformation of metals and alloys. Although dislocation distributions are rather uniform at the onset of plastic deformation, they usually become unstable when deformation proceeds and undergo successive transitions towards various types of microstructures such as cells, deformation bands, persistent slip bands, labyrinth structures, etc. However, and despite the development of a wide range of theoretical investigations and modeling approaches, many intriguing and open questions still exist.

During the past few decades, two distinct approaches have emerged in an attempt to provide a satisfactory description of plastic instabilities, and in particular, shear band formation. The first approach is based on the idea that the instabilities are geometric in origin, in much the same way as that of Euler buck-

ling of a slender beam, where changes in geometry are necessary at some critical stress level. This idea is explored through the solution of field equations, within what is known as crystal plasticity framework, and the condition for the onset of the instability is obtained as a bifurcation in the solution at some critical conditions of stress, geometry or material parameters. This approach is devoid of any physical content, and does not provide any insight into the physical nature of plastic instabilities. On the other hand, several approaches utilize a description of plastic deformation on the basis of rate equations that describe the evolution of the dislocation microstructure. The second approach has been pursued without consideration of the geometric aspects of deformation, as embodied in the first approach. In this thesis, we combine, for the first time, the physical aspects of plastic deformation, as represented by dislocation evolution equations, with the mechanical description of crystal plasticity.

The present research has provided a methodology for including physical dislocation mechanisms of plastic deformation into the framework of finite element crystal plasticity. As such, we have shown that this framework is successful in predicting the formation of localized shear bands in single crystals, and that such shear bands are initiated from small imperfections in the crystal. On the other hand, differences in crystal orientations and the geometric restrictions on grain boundary sliding have been shown to initiate shear bands in bi-crystals and in polycrystals. The spatial distribution of local plastic shear strain has been shown to be quite heterogeneous within grains, even though the applied strain is initially uniform in the crystal. We have also studied some of the aspects of $3D$ single crystal deformation model with 12 slip systems, and have shown the main characteristics related to activation of shear on various slip systems. Future work may be able to shed more light on the physical origins of plastic instabilities in 3D crystals with more advanced dislocation models.

References

[1] R. J. Amodeo and N. M. Ghoniem. Dislocation dynamics. i. a proposed methodology for deformation micromechanics. *Phys. Rev. B*, 41:6958, 1990.

[2] L. Anand and S. R. Kalidindi. The process of shear bans formation in plane strain compression of fcc metals: effect of crystallographic texture. *Mech. Mater.*, 17, 1994.

[3] L. Anand and M. A. Kathari. A computational procedure for rate-independent crystal plasticity. *Journal of the mechanics and physics of solids*, 44, 1996.

[4] A. S. Argon and W. Moffatt. Stead-state creep of alloys due to viscous motion of dislocations. *Acta Metallurgica*, 29:293, 1981.

[5] R. J. Asaro and A. Needelman. Texture development and strain hardening in rate dependent polycrystals. *Acta Metall.*, 33, 1985.

[6] R. J. Asaro and J. R. Rice. Strain localization in ductile single crystals. *J. Mech. Phys. Solids*, 25:309–338, 1977.

[7] R. J. Asaro. Crystal plasticity. *ASME J. Appl. Mech.*, 50:921–934, 1983.

[8] R. J. Asaro. Micromechanics of crystal and polycrystals. *Adv. Appl. Mech.*, 23:1–115, 1983.

[9] M. F. Ashby. The influence of particles on boundary mobility. *Proc. 1st Riso Int. Symp. on Metallurgy and Materials Science Recrystallization and Grain Growth of Multi-Phase and Particle Containing Materials.*, 1980.

[10] R. I. Borja and J. R. Wren. Discrete micromechanics of elastoplastic crystal. *International Journal for Numerical Methods in Engineering*, 36:3815–3840, 1993.

[11] C. A. Bronkhorst, S. R. Kalidindi, and L. Anand. Polycrystal plasticity and evolution of crystallographic texture in face-centered cubic metals. *Phil. Trans. Royal Soc. London A*, 341:443–477, 1992.

[12] R. Bullough, M. W. Finnis, and M. H. Wood. *Journal of Nuclear Materials*, 103:1263, 1981.

[13] W. D. Jr. Callister. *Material Science and Engineering An Introduction.* John Wiley and Sons, Inc., 1999.

[14] Jesper Vejlø Cartensen. Structural evolution and mechanisms of fatigue in polycrystalline brass. (RisØ-R-1005(EN)), 1998.

[15] K. D. Challenger and J. Moteff. *Metall Trans*, 4:749, 1973.

[16] A. H. Cottrell. *Prog. Metall. Physics*, 1:77, 1952.

[17] I. J. Cuddy. *Metall Trans*, 1:395, 1970.

[18] A. M. Cuitiño and M. Ortiz. *Modelling and Simulation in Materials Science and Engineering*, 1:225–263, 1992.

[19] P. R. Dawson, D. P. Mika, and N. R. Barton. Finite element modeling of lattice misorientations in aluminum alloys. *Scripta Materialia*, 47:713–717, 2002.

[20] I. L. Dillamore and J. G. Roberts. Occurrence of shear bands in heavily rolled cubic metals. *J. Metal Sci.*, 13:73–77, 1979.

[21] C. F. Elam. *Proc. R. Soc. London*, A115:133, 1927.

[22] U. Essmann and H. Mughrabi. Annihilation of dislocations during tensile and cyclic deformation and limits of dislocation densities. *Philosophical Magazine*, 40(6), 1979.

[23] J. A. Ewing and W. Rosenhain. *Philios. Trans. R. Soc. London*, 193:353–375, 1900.

[24] J. Friedel. *Dislocations*. Addison-Wesley Publishing Company, Inc., 1964.

[25] N. M. Ghoniem, J. R. Matthews, and R. J. Amodeo. A dislocation model for creep in engineering materials. *Res Mechanica*, 29:197–219, 1990.

[26] J. H. Gittus. Multiaxial mechanical equation of states for a work-hardening/recovery model of dislocation creep. *Philosophical Magazine*, 25:1233, 1972.

[27] J. H. Gittus. Theoretical value of the ratio (k) of cell diameter to dislocation spacing for a material undergoing dislocation-creep. *Philosophical Magazine*, 34:293, 1977.

[28] J. H. Gittus. Theoretical ralationship between free energy and dislocation cell diameter during creep. *Philosophical Magazine*, 39:829, 1979.

[29] J. Gittus. The mechanical equation of states: Dislocation creep due to stresses varying in magnitude and direction. *Philosophical Magazine*, pages 1423–1440, 1971.

[30] A. G. Guy. *Essentialas of Materials Science*. McGraw-Hill Book Company, New York, 1976.

[31] R. Hill and J. R. Rice. Constitutive analysis of elastic-plastic crystals at arbitary strain. *J. Mech. Phys. Solids*, 20:401–413, 1972.

[32] R. Hill. Generalized constitutive relations for incremental deformation of metal crystals by multislip. *J. Mech. Phys. Solids*, 14:95–102, 1966.

[33] J. P. Hirth and J. Lothe. *Theory of Dislocations*. John Wiley and Sons, Inc., 1982.

[34] J. P. Hirth, M. Rhee, and H. M. Zbib. Modeling of deformation by a 3d simulation of multiple, curved dislocations. *J. Comput.- aided Mater. Des.*, 3:164, 1996.

[35] Y. Huang, H. Gao, W. D. Nix, and J. W.Hutchinson. Mechanism-based strain gradient plasticityii. analysis. *Mechanics and Physics of Solids*, 48:99128, 2000.

[36] ABAQUS Inc. Abaqus 6.5 documentation, analysis manual. 2005.

[37] W. G. Johnson and J. J. Gilman. *Journal of Applied Physics*, 30:129, 1950.

[38] R. D. Kreig and D. B. Kreig. Accuracies of numerical solution methods for the elastic-perfectlt plastic model. *Journal of Pressure Vessel Technology*, 99, 1977.

[39] L. P. Kubin and G. R. Canova. The modelling of dislocation patterns. *Scripta Metall. Mater.*, 27, 1992.

[40] R. Lagneborg, B. H. Forsen, and J. Wiberg. A recovery-creep model based upon dislocation distributions. *The Materials Society, London*, pages 1–7, 1974.

[41] T. G. Langdon. Dislocations and creep. *Proc. Conf. on Dislocations and the Properties of Real Materials, Royal Society of London*, page 221, 1984.

[42] J. Lepinoux and L. P. Kubin.

[43] D. G. Luenberger. *Linear and Nonlinear Programming*. Addison-Wesley, 1984.

[44] J. Mandel. Generalisation de la throie de la plasticite de w. t. koiter. *Int. J. Solids Struct*, 1:273–295, 1965.

[45] E. B. Marin and P. R. Dawson. Elastoplastic finite element analyses of metal deformation using polycrystal constitutive models. *Computer methods in applied mechanics and engineering*, 165:23–41, 1998.

[46] D. J. Michel, J. Moteff, and A. J. Lovell. Substrucuture of type 316 stainless steel deformed in slow tension at temperatures between 21 c and 816 c. *Acta Metallurgica*, 21:1269, 1973.

[47] C. Miehe and J. Schroder. A comparative study of stress update algorithms for rate-independent and rate-dependent crystal plasticity. *International Journal for Numerical Methods and Engineering*, 50:273–298, 2001.

[48] K. Morii and Y. Nakayama. *Trans. Japan Inst. Metals*, 22:857–864, 1981.

[49] Ortiz M and L. Stainier. The variational formulation of viscoplastic constitutive updates. *Computer Methods in Applied Mechanics and Engineering*, 171:419–444, 1999.

[50] F. R. N. Nabarro. Steady-state diffusional creep. *Philosophical Magazine*, page 231, 1967.

[51] E. Orowan. Uber den mechanismus des gleituorganges. *Z. Phys*, 89, 1934.

[52] D. Peirce, R. J. Asaro, and A. Needelman. An analysis of nonuniform and localized deformation in ductile single crystals. *Acta Metall*, 30, 1982.

[53] M. Von Polanyi. Uber eine art gitterstorung, die einen kristall plastisch machen konnte. *Z. Phys*, 89:411–416, 1934.

[54] W. H. Press, B. P. Flannery, S. A. Teukolsky, and W. T. Vetterling. *Numerical Recipes*. Cambridge Univerisity Press, 1986.

[55] F. B. Prinz and A. S. Argon. The evolution of plastic resistance in large strain plastic flow of single phase subgrain forming metals. *Acta Metallurgica*, 32:1021–1028, 1984.

[56] H. Rauh and R. Bullough. *Philosophical Magazine*, 52:33, 1985.

[57] J. R. Rice. Inelastic constitutive relations for solids: an internal variable theory and its applcation to metal plasticity. *J. Mech. Phys. Solids*, 19:433–455, 1971.

[58] Rolf Sandstrom. On recovery of dislocations in subgrains and subgrain coalescence. *Acta Metallurgica*, 25:897–904, 1977.

[59] Rolf Sandstrom. Subgrain growth occurring by boundary migration. *Acta Metallurgica*, 25:905–911, 1977.

[60] E. Schmid. *Proc. Int. Congr. Appl. Mech. (Drift)*, page 342, 1924.

[61] J. Schröder and C. Miehe. Aspects of computational rate-independent crystal plasticity. *Computational Materials Science*, 9:168–176, 1997.

[62] K. W. Schwart. Interaction of dislocations on crossed glide planes in a strained epitaxial layer. *Phys. Rev. Lett.*, 78:4785, 1997.

[63] J. C. Simo and T. J. R Hughes. *Computational Inelasticity*. Springer, 1998.

[64] J. C. Simo, J. G. Kennedy, and S. Govindjee. Non-smooth multisurface plasticity and viscoplasticity. loading/unloading conditions and numerical algorithms. *International Journal for Numerical Methods in Engineering*, 26:2161–2185, 1988.

[65] B. N. Singh, D. J. Ewards, and S. Tahtinen. Final report on in-reactor tensile tests on ofhc-copper and cucrzr alloy. (RisØ-R-1481(EN)), 2004.

[66] S. Takeuchi and A. S. Argon. Steady-state creep of single-phase crystalline matter at high temperature. *Journal of Applied Materials Science*, 11:1542–1566, 1976.

[67] S. Takeuchi and A. S. Argon. Stead-state creep of alloys due to viscous motion of dislocations. *Acta Metallurgica*, 24:883, 1976.

[68] G. I. Taylor and C. F. Elam. The distortion of an alumnium cyrstal during a tensile test. *Proc. Royal Soc. London A*, 102:643–667, 1923.

[69] G. I. Taylor and C. F. Elam. The plastic extension and fracture of aluminum single crystals. *Proc. Royal Soc. London A*, 108:28–51, 1925.

[70] G. I. Taylor. The mechanism of plastic deformation of crystals. *Part I. - theoretical Proc. R. Soc. London. Sec. A*, 145:362–387, 1934.

[71] G. I. Taylor. Analysis of plastic strain in a cubic crystal. *Stephen Timenoshenko 60th Aniversary Volume*, pages 218–224, 1938.

[72] G. I. Taylor. Plastic strain in metals. *J. Institute of Metals*, 62:307–324, 1938.

[73] H. S. Turkmen, P. R. Dawson, and M. P. Miller. The evolution of crystalline stresses of a ploycrystalline metal during cyclic loading. *International Journal of Plasticity*, 18:941–969, 2002.

[74] H. S. Turkmen, R. E. Loge, P. R. Dawson, and M. P. Miller. On the mechanical behavior of aa 7075-t6 during cyclic loading. *Internaition Journal of Fatigue*, 25:267–281, 2003.

[75] E. Voce. *Inst Metals*, 74:537, 1948.

[76] Z. Q. Wang, N. M. Ghoniem, S. Swaminarayan, and R. Lesar. A parallel algorithm for 3d dislocation dynamics. *Journal of Computational Physics*, 219:608–621, 2006.

[77] Z. Wang. *Large Scale Dislocation Dynamics Simulation of Bulk Deformation*. PhD thesis, Univeristy of California, Los Angeles, 2004.

[78] G. A. Webster. *Philosophical Magazine*, 14:775, 1966.

[79] G. Wilkins. Calculation of elastic-plastic flow. *Methods of Computational Physics*, 1964.

[80] *ASM Handbook*, volume 2. 2000.